Posted on 25 May 2023 — The copyright holder is the author/funder. All rights reserved. No reuse without permission. — https://doi.org/10.22541/essoar.168500333.32741884/v1 — This a preprint and has not been peer reviewed. Data may be preliminary.

Ionospheric Flow Vortex Induced by the Sudden Decrease in the Solar Wind Dynamic Pressure

Yaqi Jin[1], Jøran Idar Moen[2], Andres Spicher[3], Jianjun Liu[4], Lasse Boy Novock Clausen[1], and Wojciech Jacek Miloch[1]

[1]University of Oslo
[2]University Centre in Svalbard, Longyearbyen, Norway
[3]UiT The Arctic University of Norway
[4]Polar Research Institute of China

May 25, 2023

Abstract

Abrupt changes in the solar wind dynamic pressure can greatly affect the Earth's magnetosphere-ionosphere system. We present an ionospheric flow vortex in the morning side during the sudden decrease in the solar wind dynamic pressure. The flow vortex was clearly observed by both the Hankasalmi radar and the azimuthal scan mode of the European Incoherent Scatter (EISCAT) Svalbard Radar (ESR). The flow vortex was first seen in the eastern field of view (FOV) of the Hankasalmi radar, and then propagated poleward and westward into the FOV of the ESR. During the passage of the flow vortex, a gradual decrease of electron density was observed by the field-aligned ESR 42 m antenna. When the equatorward directed ionospheric flow reached the ESR site, weak and visible increases in the electron density and electron temperature were observed. This impact was likely caused by soft electron precipitation associated with the clockwise flow vortex and upward field-aligned current. The azimuthal scan mode of the ESR 32 m radar at low elevation angle (30°) allowed us to measure key ionospheric parameters over a larger area (6° in latitude and 120° in azimuthal angle). The latitudinal scan of the electron temperature was used to derive the equatorward auroral boundary, which shows that the flow vortex was located in the subauroral region. We further demonstrated that it is possible to study the weak increase of electron density by using GPS total electron content (TEC) data. A minor TEC increase was observed near the center of the flow vortex.

Ionospheric Flow Vortex Induced by the Sudden Decrease in the Solar Wind Dynamic Pressure

Yaqi Jin[1], Jøran Idar Moen[1,2], Andres Spicher[3], Jianjun Liu[4], Lasse B. N. Clausen[1], and Wojciech J. Miloch[1]

[1]Department of Physics, University of Oslo, Oslo, Norway

[2]University Centre in Svalbard, Longyearbyen, Norway

[3]Department of Physics and Technology, UIT the Arctic University of Norway, Tromsø, Norway

[4]SOA Key Laboratory for Polar Science, Polar Research Institute of China, Shanghai, China

Corresponding author: Yaqi Jin (yaqi.jin@fys.uio.no)

Key Points:

- An ionospheric flow vortex is likely triggered by the sudden decrease in the solar wind dynamic pressure
- The flow vortex caused a reduction of the electron density
- In the morning sector, the flow vortex is clockwise and associated with upward field-aligned current and downward electron precipitation

Abstract

Abrupt changes in the solar wind dynamic pressure can greatly affect the Earth's magnetosphere-ionosphere system. We present an ionospheric flow vortex in the morning side during the sudden decrease in the solar wind dynamic pressure. The flow vortex was clearly observed by both the Hankasalmi radar and the azimuthal scan mode of the European Incoherent Scatter (EISCAT) Svalbard Radar (ESR). The flow vortex was first seen in the eastern field of view (FOV) of the Hankasalmi radar, and then propagated poleward and westward into the FOV of the ESR. During the passage of the flow vortex, a gradual decrease of electron density was observed by the field-aligned ESR 42 m antenna. When the equatorward directed ionospheric flow reached the ESR site, weak and visible increases in the electron density and electron temperature were observed. This impact was likely caused by soft electron precipitation associated with the clockwise flow vortex and upward field-aligned current. The azimuthal scan mode of the ESR 32 m radar at low elevation angle (30°) allowed us to measure key ionospheric parameters over a larger area (6° in latitude and 120° in azimuthal angle). The latitudinal scan of the electron temperature was used to derive the equatorward auroral boundary, which shows that the flow vortex was located in the subauroral region. We further demonstrated that it is possible to study the weak increase of electron density by using GPS total electron content (TEC) data. A minor TEC increase was observed near the center of the flow vortex.

1 Introduction

The Earth's magnetosphere-ionosphere system can be greatly affected by abrupt changes in the solar wind dynamic pressure. For example, the sudden increase in the solar wind dynamic pressure associated with a fast interplanetary shock can cause significant compression of the magnetosphere. Consequently, a positive geomagnetic sudden impulse (SI+) can be observed using ground-based magnetometers (e.g., Araki, 1994). Several phenomena can result from the compression of the magnetosphere. For example, the intensification of auroral luminosity can be found first near local noon, and then the intensification propagates to the nightside along the dawn and dusk flanks of the auroral oval (Zhou & Tsurutani, 1999; Zhou et al., 2003; Meurant et al., 2003). The sudden increase of the solar wind dynamic pressure can also induce travelling convection vortices (TCVs), which are east-west aligned pairs of oppositely-directed flow vortices (Friis-Christensen et al., 1988). Once generated, the TCVs propagate tailward away from local noon in the high-latitude ionosphere with a speed of several km/s (Friis-Christensen et al., 1988; Glassmeier et al., 1989; Lühr et al., 1996). The ionospheric flow vortices associated with TCVs have been observed by incoherent scatter radars (Lühr et al., 1996; Valladares et al., 1999) and Super Dual Auroral Radar Network (SuperDARN) radars (Lyatsky et al., 1999; Kataoka et al., 2003; Liu et al., 2011).

Though there exist many studies on the ionospheric effect due to the sudden solar wind pressure increase in the literature (Zou et al., 2017; Schunk et al., 1994; Collis & Haggstrom, 1991), studies on the impact of negative solar wind pressure pulses and magnetosphere expansion are quite rare. Early studies focused on the magnetic field perburbations related to the dynamic pressure decrease (Araki & Nagano, 1988; Takeuchi et al., 2002a). More recently, by using the SuperDARN King Salmon radar, Hori et al. (2012) reported poleward propagating vortex-like flow structures in the evening sector (~19 magnetic local time (MLT)) which were induced by a negative sudden impulse of the solar wind pressure. In another study, Zhao et al. (2016) reported a magnetospheric flow vortex that was driven by a negative solar wind dynamic pressure pulse. It has been found that the direction of the flow vortex was opposite to the scenario due to positive solar wind pressure pulses. By using the ground-based all-sky imager, the enhancement of the auroral luminosity has been found in the dawnside (~5 MLT) ionosphere in associated with an upward field-aligned current (FAC) (Zhao et al., 2019).

Besides the sudden changes in the solar wind dynamic pressure, another important mechanism that transfers momentum and energy to the magnetosphere-ionosphere system is magnetic reconnection (Dungey, 1961). The flux transfer event (FTE) is used to describe the transient, pulsed reconnection at the dayside magnetopause (Haerendel et al., 1978; Russell & Elphic, 1978, 1979; Lockwood & Hapgood, 1998). Southwood (1987) proposed a model to explain the ionospheric signatures of FTEs. In the Southwood model, a pair of field-aligned currents (FACs) with opposite direction is generated on the

poleward and equatorward edge of the newly reconnected flux tube. The pair of FACs sets up a twin vortex flow pattern on both sides of the newly reconnected flux tube. Later, by using the fast azimuth sweeps of the EISCAT Svalbard radar (ESR), Rinne et al. (2007) found that the return flow of the newly reconnected flux never formed simultaneously in pairs. As a result, an asymmetric version of the Southwood FTE model was proposed, where the return flow only occurs on the poleward side of the newly reconnected flux tube and this was termed as reversed flow event (RFE) (Rinne et al., 2007; Moen et al., 2008).

In this study, we report an event of ionospheric flow vortex in the morning side ionosphere. As will be shown later, this event is likely driven by an abrupt, step function like decrease in the solar wind dynamic pressure. The used instruments and datasets are introduced in section 2. Section 3 presents the event in detail, following by a summary and discussion in section 4.

2 Instrumentation and dataset

In this study, we use the European Incoherent Scatter (EISCAT) Svalbard Radar (ESR) in Longyearbyen, the SuperDARN radar in Hankasalmi, Finland, and Global Positioning System (GPS) receiver in Ny-Ålesund.

The ESR in Longyearbyen (78.15°N, 16.02°E; magnetic latitude (MLAT) 75.43°N) consists of a 32-m steerable antenna and a 42-m static field-aligned antenna (azimuth = 182.1°, elevation = 81.6°). The basic ionospheric properties such as the electron density (Ne), electron temperature (Te), ion temperature (Ti), and line-of-sight ion velocity (Vi) can be obtained from both antennas (e.g., Wannberg et al., 1997). On 3 December 2011, the ESR 32 m antenna was operated in a fast azimuth scan mode from 6:30 to 8:30 UT to study the RFEs (Carlson et al., 2002; Rinne et al., 2007). The 32-m antenna beam moved between azimuth angles of 180° and 300° at an elevation angle of 30° and was alternating between clockwise and anticlockwise motion. With the highest allowed azimuthal scan speed of 0.625°/s, the radar beam completes one 120° azimuthal scan in 192 s. The selected pulse code *taro* allows for simultaneous transmission and receiving of signals by both antennas. The stored data resolution is 6.4 s, which results in 30 adjacent radar beam directions in one complete azimuthal scan. For the data from the ESR 42 m antenna, the data are analyzed using GUISDAP with integration time of 64 s.

For the ionospheric drift velocities, we use the data from the coherent scatter high frequency (HF) radar in Hankasalmi (62.3°N, 26.6°E) from SuperDARN (Milan et al., 1999; Greenwald et al., 1995). The HF radar operates in 16 azimuthal beams that are separated by about 3.2°. By analyzing the backscatter echoes from field-aligned ionospheric irregularities, the line-of-sight Doppler drift velocity, spectral

width, and power can be obtained. We use the SuperDARN data at the FITACF level, which is a commonly used routine to process SuperDARN auto-correlation functions (see e.g., Ribeiro et al., 2013).

The solar wind data from the OMNI database are used to present the upstream solar wind conditions (King & Papitashvili, 2005). The OMNI interplanetary magnetic field (IMF) is presented in the geocentric solar magnetospheric coordinates. The Sym-H index and AE indices in 1-min resolution is used to show the global magnetic response to the solar wind variations. The Sym-H and AE indices were obtained from the World Data Center for Geomagnetism at Kyoto University (http://wdc.kugi.kyoto-u.ac.jp/).

The GPS data in Ny-Ålesund (78.9°N, 11.9°E) is taken from the International Global Navigation Satellite System (GNSS) Service. The Receiver Independent Exchange Format (RINEX) format data in 1-s resolution is downloaded from the high-rate data of NASA's Crustal Dynamics Data Information System (CDDIS) https://cddis.nasa.gov/archive/gnss/data/highrate/. The carrier phase observations at L1 and L2 bands are used to calculate the total electron content (TEC). In this study, we only use 1-s resolution TEC data from GPS satellite 31.

3 Results

The event was observed on December 3, 2011 during the EISCAT campaign for the Norwegian sounding ICI-3 rocket (Spicher et al., 2016; Jin et al., 2017; Jin et al., 2019). Figures 1a-c present the upstream solar wind and IMF information from the OMNI dataset. The solar wind density (Figure 1a) decreased abruptly from 13 cm^{-3} at 6:39 UT to 3 cm^{-3} at 6:42 UT. This resulted in a sharp decrease in the solar wind dynamic pressure (P_{dyn}) from 4.9 nPa to slightly below 1 nPa (Figure 1b). The IMF was characterized by a sharp southward turn from 6:37 UT to 6:41 UT. The IMF By remained negative with decreasing magnitude. The AU, AL and AE indices are shown in Figure 1d. The AL index was relatively stable, while AE and AU slightly increased from ~6:39 UT. The Kp index was stable at 2+, while the Sym-H index decreased quickly from 6:39 UT. The decrease of the Sym-H index was a response of the decrease of solar wind dynamic pressure and a decrease of the magnetopause current (Takeuchi et al., 2002b). We therefore consider 6:39 UT as the time when the solar wind pressure decrease arrived at the dayside magnetosphere.

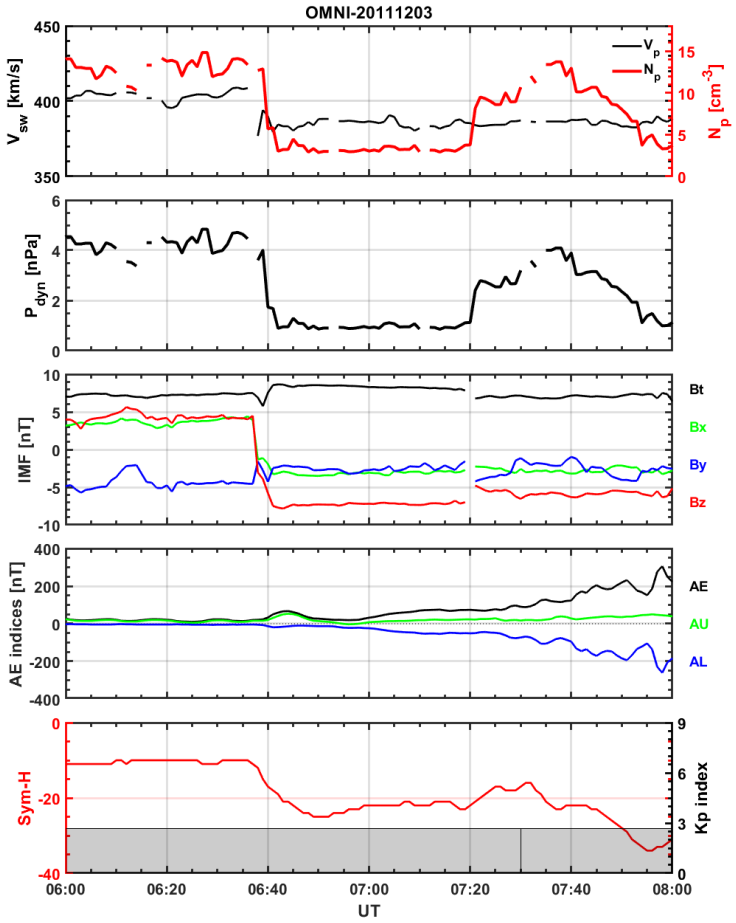

Figure 1. An overview of the solar wind, IMF, AE, Sym-H, and Kp indices from 6:00 to 8:00 UT on 3 December 2011. (a) The solar wind velocity (black) and proton density (Np, red); (b) the solar wind dynamic pressure; (c) the IMF strength (Bt, black), By (blue), and Bz (red) components; (d) AU (green), AL (blue), and AE (black) indices; (e) the Sym-H (red) and Kp (black shaded) indices. IMF = Interplanetary Magnetic Field.

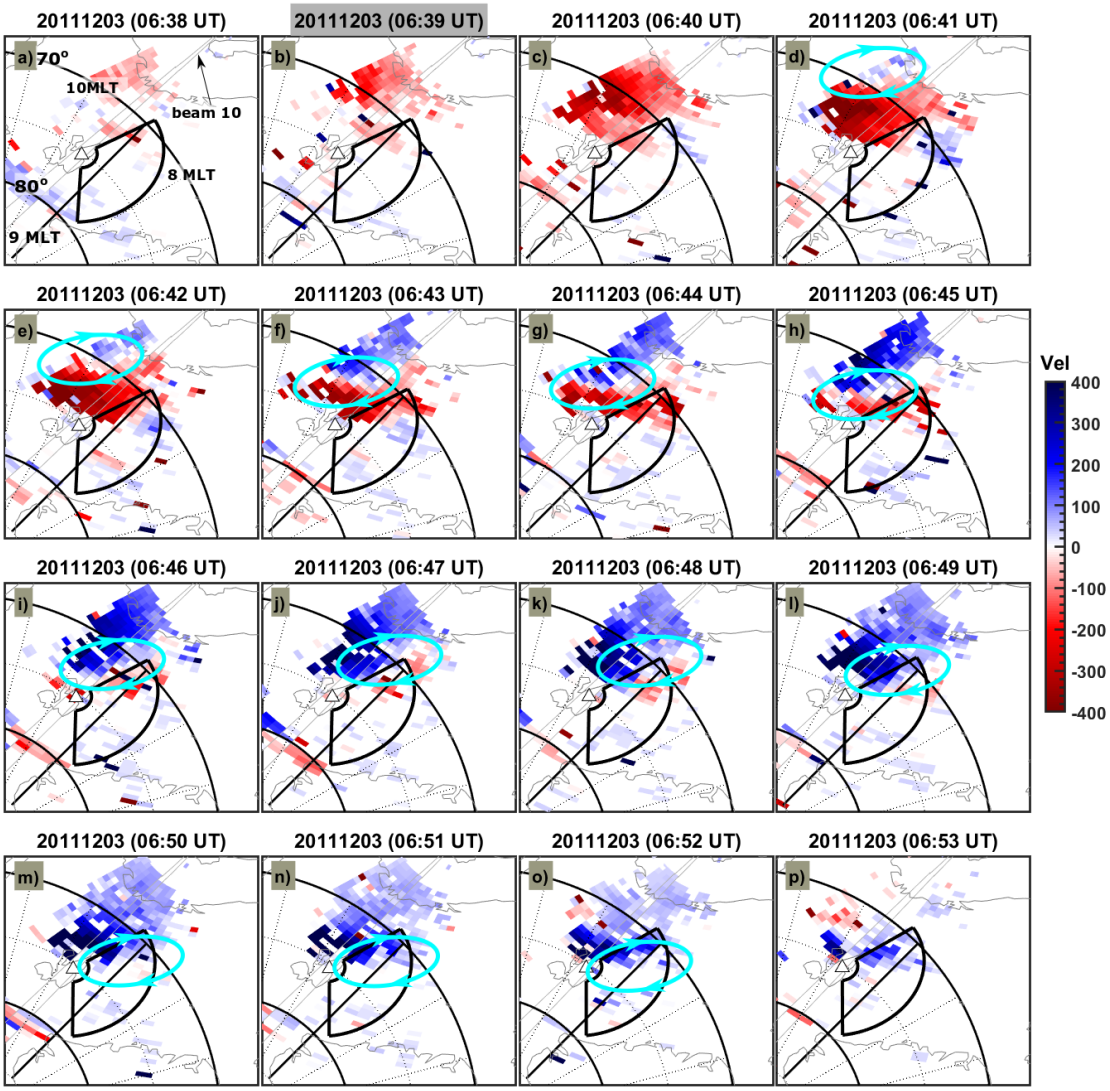

Figure 2. The Doppler drift velocity observed in the field-of-view of the Hankasalmi HF radar with the time cadence of 1 min. The data is presented in MLAT/MLT coordinates, with magnetic noon to the top an dawn to the right. In each panel, the radar beam 10 is marked. The black fan-shaped area is the field-of-view of the ESR 32 m antenna. The white triangle is the location of ESR in Longyearbyen. The enhanced poleward ionospheric flow was first visible at 06:39 UT.

Figure 2 shows the Doppler drift velocity in the field-of-view (FOV) of the Hankasalmi HF radar. The radar FOV was located in the morning sector (8-10 MLT). The enhanced poleward (red) ionospheric flow was first observed in the eastern side of the FOV around 68° MLAT and 10 MLT (Figure 2b). Then the enhanced flow moved poleward and tailward toward earlier MLT. The first equatorward directed flow was observed at 6:41 UT (Figure 2d). This was a clockwise flow vortex as annotated by the arrowed cyan ellipse. The whole vortex flow moved westward and entered the FOV of the scan mode of the ESR 32 m antenna (as indicated by the black fan-shaped area on the westside of Svalbard. The data from ESR 42 m

beam (field-aligned in the F region, azimuth 182.1°, elevation 81.6°) is also available. The ESR radar site is annotated by a white triangle in each panel of Figure 2.

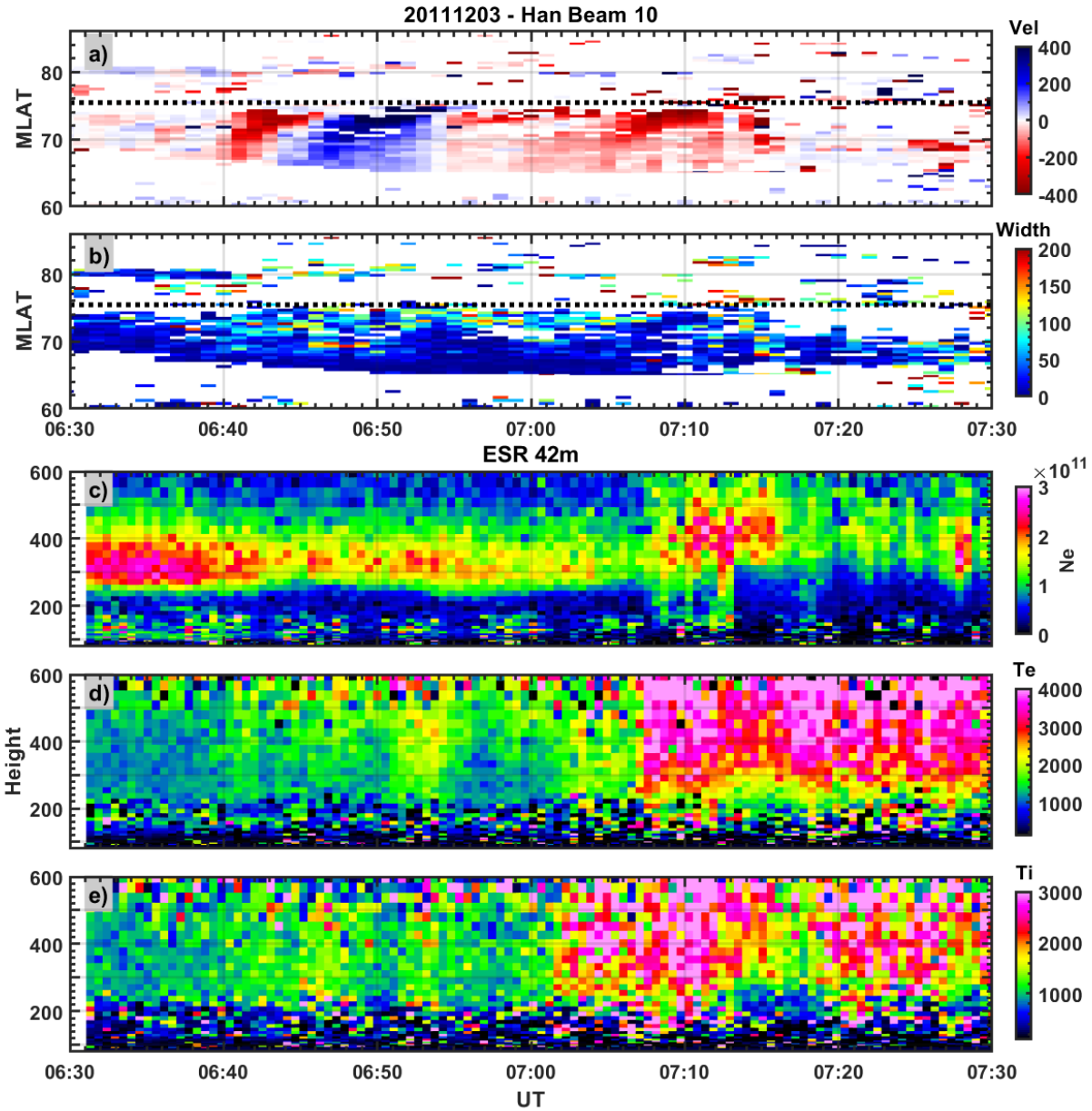

Figure 3. Ionospheric data from the Hankasalmi HF radar and the EISCAT 42 m antenna. The Doppler drift velocity (a) and spectral width (b) from beam 10 of the Hankasalmi HF radar as a function of magnetic latitude (MLAT). The black horizontal dashed line shows the location of the ESR 42 m radar at 75.43° MLAT. The altitude profiles of electron density (c), electron temperature (d), ion temperature (e) from the field-aligned 42 m antenna.

The radar beam 10 of the Hankasalmi radar is aligned with ESR (Figure 2a). The range-time plot of data from beam 10 is presented in Figures 3a-3b, where the black dashed horizontal line shows the location of

the ESR site. Figure 3a shows that the poleward directed ionospheric flow reached ESR around 6:45 UT, while the equatorward directed flow reached the ESR site around 6:52 UT. Note that there is a lack of HF backscatter around the ESR site, which could be due to not optimal propagation ray-path of the radar signal. Figure 3b shows the spectral width from beam 10, which shows that the flow vortex was associated with slightly enhanced spectral width. We present the ionospheric data from the ESR 42 m radar in Figures 3c-3e. The electron density profile shows a region of moderate high electron density ($2.5\times10^{11}m^{-3}$) at ~250-400 km between 6:30-6:40 UT. When the flow vortex reached near the ESR site, the electron density significantly decreased to around $1.5\times10^{11}m^{-3}$. Interestingly, there was a region of slightly increase in electron density around 6:51-6:53 UT. This was at the same time when the equatorward directed flow (blue) reached the ESR site (Figure 3a). The minor increase of the electron density was also associated with the slight increase in the electron temperature. As will be discussed later, this was likely associated with an auroral arc in connection to the flow vortex (Lühr et al., 1996). We also observed weak by identifiable ion temperature associated with the flow vortex. This was likely due to the impact of enhanced ion frictional heating during enhanced ionospheric flow. We note that the ESR 42 m antenna was equatorward of the main auroral oval when the flow vortex is observed (cf. Figure 5). As the IMF Bz turned southward, the main auroral oval expanded equatorward. The main auroral oval should arrive at the ESR site at about 7:07 UT as indicated by the abrupt increase in the electron temperature (Figure 3d). The ongoing soft precipitation also caused enhanced electron density and ion temperature.

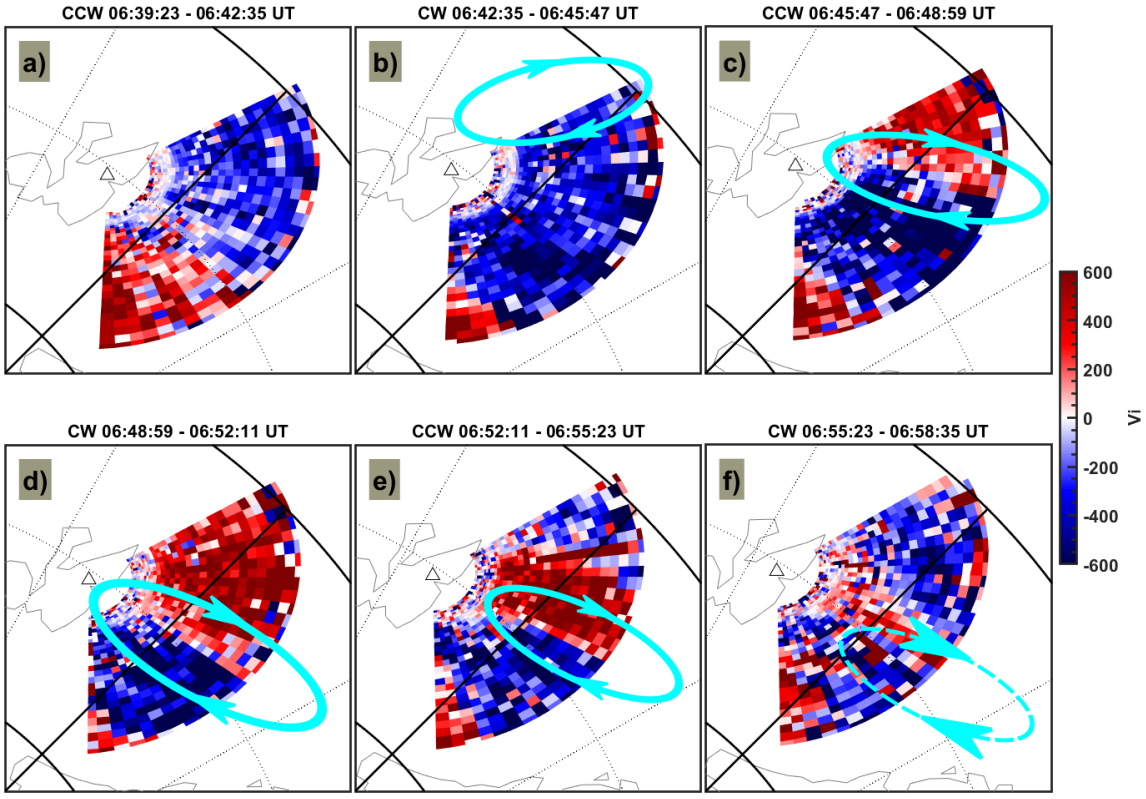

Figure 4. Line-of-sight ion velocity (Vi) observed by the ESR 32 m antenna. Positive (red) velocities are away from the radar site. The scan time is shown on the top of each panel, where "cw" is clockwise and "ccw" is counterclockwise scan. The arrowed cyan ellipse indicates the flow vortex.

The ESR 32 m radar was operating in a fast azimuthal scan mode at an elevation of 30° during this event. Figure 4 shows the ion velocity in 6 azimuthal scans, which show the evolution of the flow vortex when it entered and left the FOV of ESR. Figure 4a shows the scan before the flow vortex entered the FOV of ESR. Figure 4b shows that the poleward directed flow first entered the southern part of the ESR FOV as indicated by the toward (blue) ion velocity. The inferred flow vortex is overlaid as an arrowed cyan ellipse in each panel. The equatorward directed flow entered the FOV in Figure 4c as indicated by away (red) ion velocity from the ESR 32 m radar. The vortex flow continued moving westward and it was barely visible during the scan time in Figure 4f. The flow shear between the positive and negative ion velocity was evidently visible in Figures 4c-4e.

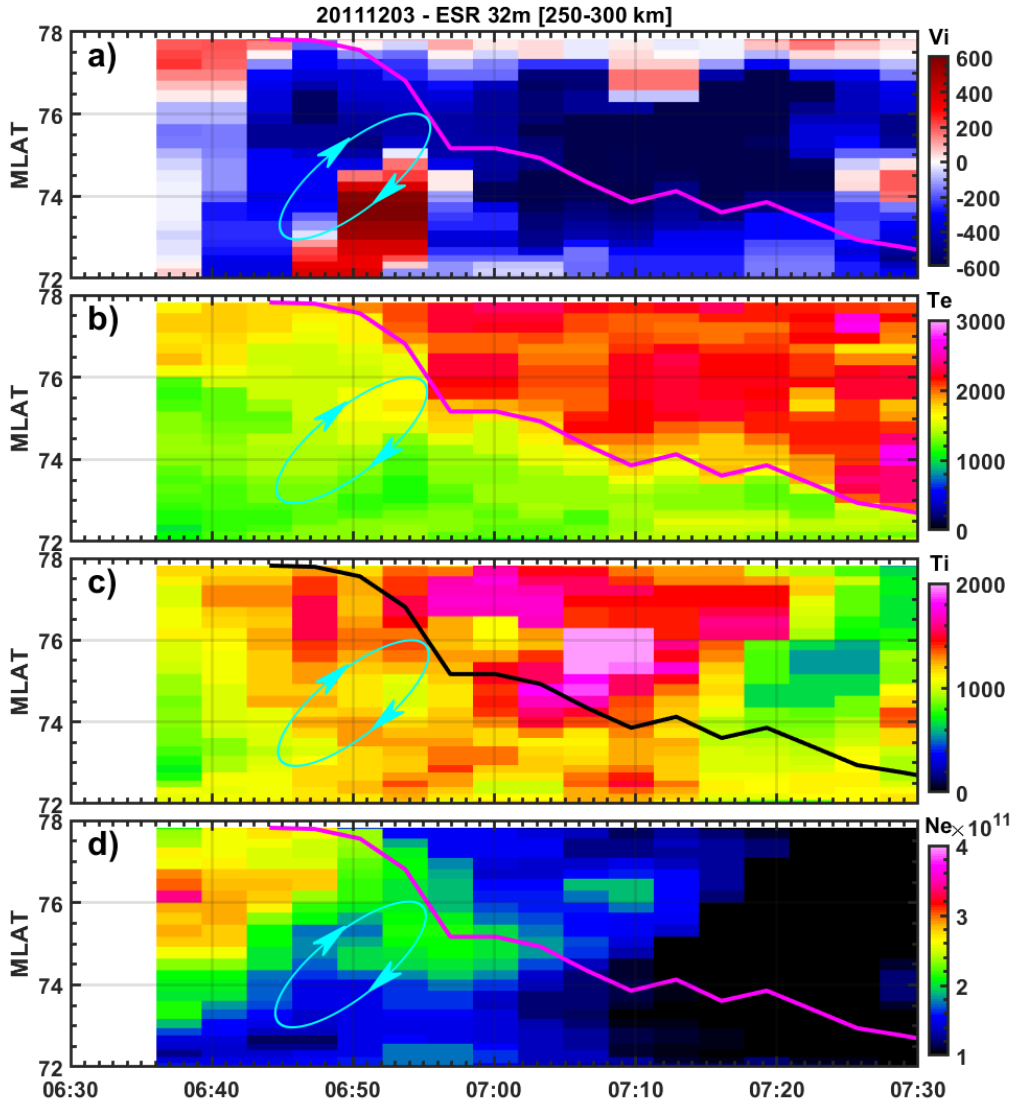

Figure 5. The ionospheric parameters obtained from the ESR 32 m antenna by averaging the data from altitudes between 250 – 300 km. Line-of-sight ion velocity (a), electron temperature (b), ion temperature (c), and electron density (d). In each panel, the magenta (black in panel c) line marks the equatorward auroral boundary as derived from the electron temperature data by selecting the equatorward boundary at Te = 1800 K. The arrowed cyan ellipse indicates the flow vortex.

It is also possible to obtain other plasma parameters from the scan mode of the ESR 32 m antenna. Figure 5 shows the ionospheric parameters from the ESR 32 m antenna, which were averaged over altitudes 250-300 km. The data were scanned along fixed range gates and are presented as a function of MLAT. As one azimuthal scan takes 192 s, the time resolution is 192 s in the horizontal axis. The flow vortex can be seen from the ion velocity from blue (toward) near 6:42 UT and red (toward) near 6:50 UT. The flow vortex is annotated by the arrowed cyan ellipse in Figure 5. Note that the measured ion velocity is line-of-sight

velocity along the radar beam, i.e., it was mainly in the north-south direction below about 74° MLAT, and it became more aligned in the east-west direction above 74° MLAT (cf. Figure 4). Figure 5b shows the electron temperature data. The latitudinal profile of electron temperature can be used to identify the auroral boundary (Doe et al., 2001). The equatorward auroral boundary was obtained by selecting the most equatorward electron temperature that exceeded 1800 K. The derived auroral boundary is plotted as a magenta line in Figures 5a-5b. The auroral boundary shifted equatorward as a response to the southward turning of the IMF Bz. The equatorward auroral boundary reached 74.3° MLAT (ESR site) at around 7:07 UT. This was consistent with the sudden increase of the electron temperature as measured by the ESR 42 m antenna around the same time (Figure 3d). This justifies that the derived equatorward auroral boundary from the electron temperature data is valid. Notice that the flow vortex was equatorward of the equatorward auroral boundary when it was observed in the FOV of the ESR 32 m antenna. Figure 5c displays the ion temperature, which shows moderate enhanced Ti in association with the flow vortex. However, the strongest ion temperature enhancement occurred in the auroral zone when there was a strong eastward flow near 75° MLAT around 7:10 UT. The averaged electron density between 250-300 km in Figure 5d shows a gradual decrease of electron density that was similar to the ESR 42 m data. Interesting, there was a weak increase of the electron density when the flow vortex was observed, and this coincided with a slight increase of the electron temperature (cf. Figure 4b).

4. Summary and Discussion

In this study, we have presented an event of ionospheric flow vortex that was triggered by a sudden decrease of the solar wind dynamic pressure. The flow vortex was observed in the morning sector (8-10 MLT and 65°-75° MLAT). The 2-D morphology of the flow vortex was clearly observed by both the Hankasalmi coherent scatter HF radar and the azimuthal scan mode of the ESR 32 m radar. The flow vortex was first seen in the eastern FOV of the HF radar, and then it propagated poleward and westward into the FOV of the ESR. When the flow vortex arrived near the ESR site, a gradual decrease of the electron density was observed by the field-aligned 42 m radar. When the equatorward directed ionospheric flow reached the ESR site, weak and visible increases in the electron density and electron temperature were observed. This impact was likely caused by soft electron precipitation associated with the flow vortex (Lühr et al., 1996; Doe et al., 2001). The azimuthal scan mode of the ESR 32 m radar at low elevation angle (30°) allowed us to measure key ionospheric parameters over a larger area (6° in MLAT and 120° in azimuthal angle). Velocity shear associated with the flow vortex was clearly visible in 3 scans (3×192 s = 9.6 min). The latitudinal scan of the electron temperature at 250-300 km was obtained in order to derive the equatorward auroral boundary. Apparently, the flow vortex was located in the subauroral region in the morning sector (cf. Figure 5). This is consistent with the studies of magnetic

signature of TCVs, i.e., the TCV center is located in the closed field line within the region of plasmasheet (Moretto & Yahnin, 1998).

As it often happens, the sudden decrease of the solar wind dynamic pressure occurred in association with the orientation change of the IMF, i.e., the sudden decrease in the solar wind dynamics pressure was associated with a southward turning of the IMF Bz. However, we can rule out the contribution of the southward turning of the IMF due to two reasons: 1) the flow vortex occurred equatorward of the auroral boundary, and it originated at lower latitudes and moved poleward and westward; while the FTE induced flow occurs near the open/closed field line boundary and propogates poleward; 2) the FTE driven flow is poleward during negative Bz (Southwood, 1987; Cowley & Lockwood, 1992), and this contradicts with the equatorward directed flow in the flow vortex. Note that this is also different from the reversed flow event (RFE) in the cusp ionosphere (Rinne et al., 2007; Moen et al., 2008; Jin et al., 2019). The RFE is interpreted as the return flow on the poleward side of the newly reconnected flux tube in the cusp region (see Figure 7 in Jin et al., 2019). On the contrary, the equatorward return flow of the flow vortex occurred on the equatorward side in our event. In addition, the reversed flow event occurs in the open field line region, while the present event occurred in closed field line. Actually, a series of reversed flow events were indeed observed in the cusp ionosphere later this day (see e.g., Jin et al., 2019), but they were not related to the event in this study.

There are a few studies that focused on the impact on the ionospheric response to SI+ and TCV. For example, Kataoka et al. (2003) observed transient production of F-region irregularities during the passage of TCV. Valladares et al. (1999) observed electron density depletion by a factor of two associated with a TCV event. The decreased electron density was explained by the fast ionospheric flow and ion frictional heating with subsequent increased recombination rate. In our event, we also observed a decrease of electron density (from 2.5×10^{11} m^{-3} to 1.5×10^{11} m^{-3}) during the passage of the flow vortex. The ion temperature was also enhanced. This indicates that the decrease of electron density should be related to fast fows, as suggested by Valladares et al. (1999) and Ogawa et al. (2001).

Unlike the impact of solar wind dynamic pressure increases, the impact of solar wind dynamic pressure decreases are relatively less studied in the literature. Zhao et al. (2016) observed magnetospheric flow vortex driven by a negative solar wind dynamic pressure pulse, where the observed vortex rotated in a direction opposite to the case due to positive solar wind dynamic pressure pulses. The negative solar wind pressure can induce FACs in the dawn and dusk sectors by Region 2 sense FACs, i.e., it flows out of (into) the ionosphere in the dawnside (duskside) (Zhao et al., 2016).

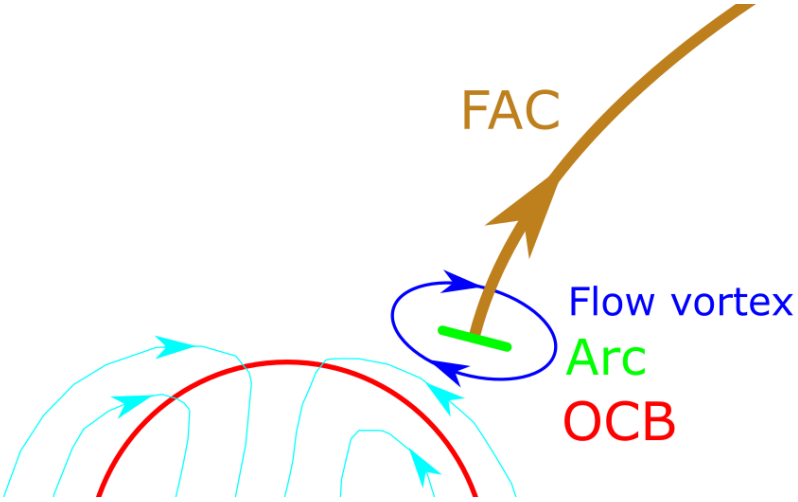

Figure 6. Sketmatics of the observation scenario. The observed clockwise ionospheric flow vortex is equatorward of the main auroral oval, and it is associated with an upward field aligned current (FAC) and downward electron precipitation. OCB = open/closed field line boundary.

Based on the previous literature and our observations, we summarize the observation scenario in Figure 6. The clockwise ionospheric flow vortex was observed in the morning side ionosphere and it was equatorward of the main auroral oval. Due to the fast flow (or flow shear) associated with the flow vortex, the electron density was significantly depleted within 10 min. The clockwise flow vortex was connected to the magnetosphere through an upward FAC, which was associated with an auroral arc due to accelerated electron precipitation. The soft precipitation caused weak enhancement of ionospheric density and electron temperature.

Given the observational feature in the ionosphere, this phenomenon should also be detectable by using ground-based GPS TEC data. For example, Jin et al. (2016) presented an event showing the global TEC response of the auroral ionosphere due to the sudden increase of the solar wind dynamic pressure associated with an interplanetary shock. The fast anti-sunward propagation of TEC enhancements due to shock-induced aurora was observed. Similarly, we show that it is also possible to detect the TEC response due to the solar wind pressure decrease by coordinated observations. Figures 7a-7b show the ion velocity, electron density and electron temperature during the azimuthal scan at 6:48:59-6:52:11 UT. The ionospheric parameters during other azimuthal scan time can be found in the supporting information. The pierce point of PRN31 tracked from Ny-Ålesund is shown as an asterisk, which was located near the flow shear during this scan. The pierce point is projected to an altitude of 300 km according to the electron density profile in Figure 3c. Figures 7b-7c show moderate electron density as well as noisy and enhanced electron temperature. Similar minor increase of the electron density and temperature can be also seen from Figures 3c-3d as well as Figures 5d and 5d. However, due to the noisiness of the ESR data, it is

difficult to conclude whether the electron density and temperature indeed increased near the flow shear. Figure 7d shows the 1-Hz resolution GPS TEC data from PRN31 (red) and its moving average (black) in a sliding window of 15 min. Clearly the TEC data shows gradual decrease from 6:40 UT onward. There was a minor increase in the TEC data from 6:48:30 UT to 6:52 UT. This was the time when PRN31 was located near the flow shear during the scan in Figures 7a-7c. The minor TEC increase (ΔTEC $\approx$ 1 TECu, where 1 TECu = 10^{16} electrons/m^2) was likely caused by auroral particle precipitation near the flow shear. This confirms that the weak increases in electron density and electron temperature by the ESR should be real. This also demonstrates that it should be possible to detect the ionospheric effect due to sudden solar wind dynamic pressure decrease by using the GPS TEC data. By using the global distributed networks of GPS receivers (Jin et al., 2016), one can investigate the propagation and evolution of the associated ionospheric effect. This provides another alternative dataset (in addition to magnetometers and optical auroral data) to study the response and evolution of the magnetosphere-ionosphere system due to the impact of the negative solar wind pressure pulse. Such studies will be explored in future investigations.

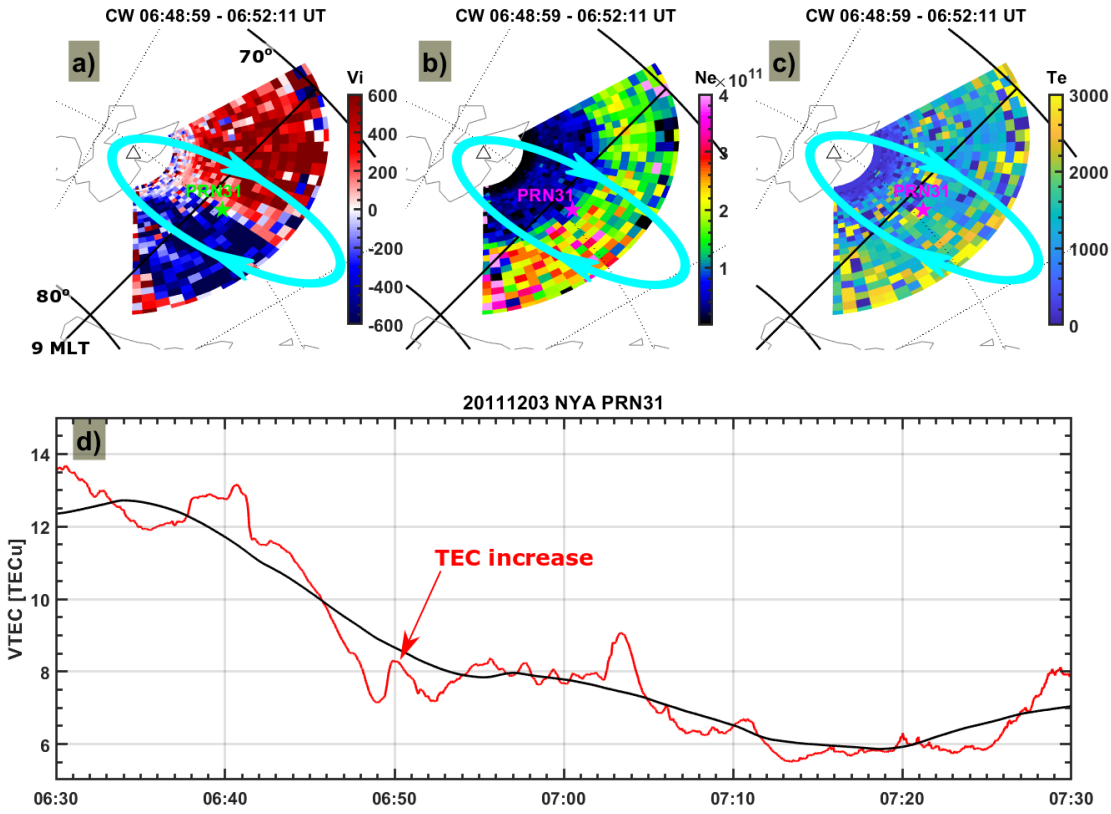

Figure 7. The observations from the ESR 32 m antenna and the vertical GPS TEC data from Ny-Ålesund (NYA). The line-of-sight ion velocity (a), electron density (b), and the electron temperature (c) from the scan of the ESR 32 m antenna. The pierce point of PRN31 at an altitude of 300 km is plotted as an

asterisk in each panel. (d) the 1-Hz resolution VTEC (red) and its moving average (black) from PRN31 tracked in Ny-Ålesund.

Acknowledgments

YJ and WJM acknowledge funding from the European Research Council (ERC) under the European Union's Horizon 2020 research and innovation programme (ERC Consolidator Grant agreement No. 866357, POLAR-4DSpace). This research is a part of the 4DSpace Strategic Research Initiative at the University of Oslo. AS acknowledges funding from the RCN grant 326039, and the UiT The Arctic University of Norway contribution to the EISCAT 3D (RCN funded grant 245683).

Open Research

The IMF and solar wind data are provided by the NASA OMNIWeb service (http://omniweb.gsfc.nasa.gov). EISCAT is an international association supported by research organizations in China (CRIRP), Finland (SA), Japan (NIPR and STEL), Norway (NFR), Sweden (VR), and the United Kingdom (NERC). Data from EISCAT can be obtained from the Madrigal database http://www.eiscat.se/madrigal. SuperDARN is a collection of radars funded by national scientific funding agencies of Australia, Canada, China, France, Japan, South Africa, United Kingdom, and the United States of America. The SuperDARN data can be obtained from http://vt.superdarn.org/tiki-index.php. The GPS data can be obtained through https://cddis.nasa.gov/archive/gnss/data/highrate/.

References

Araki, T. (1994). A Physical Model of the Geomagnetic Sudden Commencement. In *Solar Wind Sources of Magnetospheric Ultra-Low-Frequency Waves* (pp. 183-200).

Araki, T., & Nagano, H. (1988). Geomagnetic response to sudden expansions of the magnetosphere. *Journal of Geophysical Research: Space Physics, 93*(A5), 3983-3988. doi:https://doi.org/10.1029/JA093iA05p03983

Carlson, H. C., Oksavik, K., Moen, J., van Eyken, A. P., & Guio, P. (2002). ESR mapping of polar-cap patches in the dark cusp. *Geophysical Research Letters, 29*(10). doi:10.1029/2001gl014087

Collis, P. N., & Haggstrom, I. (1991). HIGH-LATITUDE IONOSPHERIC RESPONSE TO A GEOMAGNETIC SUDDEN COMMENCEMENT. *Journal of Atmospheric and Terrestrial Physics, 53*(3-4), 241-248. doi:10.1016/0021-9169(91)90108-j

Cowley, S. W. H., & Lockwood, M. (1992). Excitation and Decay of Solar Wind-Driven Flows in the Magnetosphere-Ionosphere System. *Annales Geophysicae-Atmospheres Hydrospheres and Space Sciences, 10*(1-2), 103-115. Retrieved from <Go to ISI>://WOS:A1992HL02700010

Doe, R. A., Kelly, J. D., & Sanchez, E. R. (2001). Observations of persistent dayside F region electron temperature enhancements associated with soft magnetosheathlike precipitation. *Journal of Geophysical Research-Space Physics, 106*(A3), 3615-3630. doi:Doi 10.1029/2000ja000186

Dungey, J. W. (1961). Interplanetary Magnetic Field and Auroral Zones. *Physical Review Letters, 6*(2), 47-&. doi:DOI 10.1103/PhysRevLett.6.47

Friis-Christensen, E., McHenry, M., Clauer, C., & Vennerstrøm, S. (1988). Ionospheric traveling convection vortices observed near the polar cleft: A triggered response to sudden changes in the solar wind. *Geophysical Research Letters, 15*(3), 253-256. doi:10.1029/GL015i003p00253

Glassmeier, K.-H., Hönisch, M., & Untiedt, J. (1989). Ground-based and satellite observations of traveling magnetospheric convection twin vortices. *Journal of Geophysical Research: Space Physics, 94*(A3), 2520-2528. doi:https://doi.org/10.1029/JA094iA03p02520

Greenwald, R. A., Baker, K. B., Dudeney, J. R., Pinnock, M., Jones, T. B., Thomas, E. C., . . . Yamagishi, H. (1995). Darn Superdarn - a Global View of the Dynamics of High-Latitude Convection. *Space Science Reviews, 71*(1-4), 761-796. doi:Doi 10.1007/Bf00751350

Haerendel, G., Paschmann, G., Sckopke, N., Rosenbauer, H., & Hedgecock, P. C. (1978). Frontside boundary-layer of magnetosphere and problem of reconnection. *Journal of Geophysical Research-Space Physics, 83*(NA7), 3195-3216. doi:10.1029/JA083iA07p03195

Hori, T., Shinbori, A., Nishitani, N., Kikuchi, T., Fujita, S., Nagatsuma, T., . . . Seki, K. (2012). Evolution of negative SI-induced ionospheric flows observed by SuperDARN King Salmon HF radar. *Journal of Geophysical Research-Space Physics, 117*. doi:10.1029/2012ja018093

Jin, Y., Moen, J. I., Spicher, A., Oksavik, K., Miloch, W. J., Clausen, L. B. N., . . . Saito, Y. (2019). Simultaneous Rocket and Scintillation Observations of Plasma Irregularities Associated With a Reversed Flow Event in the Cusp Ionosphere. *Journal of Geophysical Research: Space Physics, 124*(8), 7098-7111. doi:10.1029/2019ja026942

Jin, Y. Q., Moen, J. I., Oksavik, K., Spicher, A., Clausen, L. B. N., & Miloch, W. J. (2017). GPS scintillations associated with cusp dynamics and polar cap patches. *Journal of Space Weather and Space Climate, 7*. doi:10.1051/swsc/2017022

Jin, Y. Q., Zhou, X. Y., Moen, J. I., & Hairston, M. (2016). The auroral ionosphere TEC response to an interplanetary shock. *Geophysical Research Letters, 43*(5), 1810-1818. doi:10.1002/2016gl067766

Kataoka, R., Fukunishi, H., Hosokawa, K., Fujiwara, H., Yukimatu, A. S., Sato, N., & Tung, Y. K. (2003). Transient production of F-region irregularities associated with TCV passage. *Annales Geophysicae, 21*(7), 1531-1541. doi:10.5194/angeo-21-1531-2003

King, J. H., & Papitashvili, N. E. (2005). Solar wind spatial scales in and comparisons of hourly Wind and ACE plasma and magnetic field data. *Journal of Geophysical Research-Space Physics, 110*(A2). doi:10.1029/2004ja010649

Liu, J. J., Hu, H. Q., Han, D. S., Araki, T., Hu, Z. J., Zhang, Q. H., . . . Ebihara, Y. (2011). Decrease of auroral intensity associated with reversal of plasma convection in response to an interplanetary shock as observed over Zhongshan station in Antarctica. *Journal of Geophysical Research: Space Physics, 116*(A3). doi:https://doi.org/10.1029/2010JA016156

Lockwood, M., & Hapgood, M. A. (1998). On the cause of a magnetospheric flux transfer event. *Journal of Geophysical Research-Space Physics, 103*(A11), 26453-26478. doi:10.1029/98ja02244

Lyatsky, W. B., Sofko, G. J., Kustov, A. V., Andre, D., Hughes, W. J., & Murr, D. (1999). Traveling convection vortices as seen by the SuperDARN HF radars. *Journal of Geophysical Research-Space Physics, 104*(A2), 2591-2601. doi:10.1029/1998ja900007

Lühr, H., Lockwood, M., Sandholt, P. E., Hansen, T. L., & Moretto, T. (1996). Multi-instrument ground-based observations of a travelling convection vortices event. *Annales Geophysicae-Atmospheres Hydrospheres and Space Sciences, 14*(2), 162-181. doi:DOI 10.1007/s00585-996-0162-z

Meurant, M., Gérard, J.-C., Hubert, B., Coumans, V., Blockx, C., Østgaard, N., & Mende, S. B. (2003). Dynamics of global scale electron and proton precipitation induced by a solar wind pressure pulse. *Geophysical Research Letters, 30*(20). doi:https://doi.org/10.1029/2003GL018017

Milan, S. E., Davies, J. A., & Lester, M. (1999). Coherent HF radar backscatter characteristics associated with auroral forms identified by incoherent radar techniques: A comparison of CUTLASS and EISCAT observations. *Journal of Geophysical Research-Space Physics, 104*(A10), 22591-22604. doi:Doi 10.1029/1999ja900277

Moen, J., Rinne, Y., Carlson, H. C., Oksavik, K., Fujii, R., & Opgenoorth, H. (2008). On the relationship between thin Birkeland current arcs and reversed flow channels in the winter cusp/cleft ionosphere. *Journal of Geophysical Research-Space Physics, 113*(A9). doi:10.1029/2008ja013061

Moretto, T., & Yahnin, A. (1998). *Mapping travelling convection vortex events with respect to energetic particle boundaries.* Annales Geophysicae, pp. 891-899.

Ogawa, T., Buchert, S. C., Nishitani, N., Sato, N., & Lester, M. (2001). Plasma density suppression process around the cusp revealed by simultaneous CUTLASS and EISCAT Svalbard radar observations. *Journal of Geophysical Research-Space Physics, 106*(A4), 5551-5564. doi:Doi 10.1029/2000ja900111

Ribeiro, A. J., Ruohoniemi, J. M., Ponomarenko, P. V., N. Clausen, L. B., H. Baker, J. B., Greenwald, R. A., . . . de Larquier, S. (2013). A comparison of SuperDARN ACF fitting methods. *Radio Science, 48*(3), 274-282. doi:https://doi.org/10.1002/rds.20031

Rinne, Y., Moen, J., Oksavik, K., & Carlson, H. C. (2007). Reversed flow events in the winter cusp ionosphere observed by the European Incoherent Scatter (EISCAT) Svalbard radar. *Journal of Geophysical Research-Space Physics, 112*(A10). doi:10.1029/2007ja012366

Russell, C. T., & Elphic, R. C. (1978). Initial ISEE magnetometer results - magnetopause observations. *Space Science Reviews, 22*(6), 681-715. Retrieved from <Go to ISI>://WOS:A1978GM11300002

Russell, C. T., & Elphic, R. C. (1979). ISEE observations of flux-transfer events at the dayside magnetopause *Geophysical Research Letters, 6*(1), 33-36. doi:10.1029/GL006i001p00033

Schunk, R. W., Zhu, L., & Sojka, J. J. (1994). Ionospheric response to traveling convection twin vortices. *Geophysical Research Letters, 21*(17), 1759-1762. doi:https://doi.org/10.1029/94GL01059

Southwood, D. J. (1987). The Ionospheric Signature of Flux-Transfer Events. *Journal of Geophysical Research-Space Physics, 92*(A4), 3207-3213. doi:DOI 10.1029/JA092iA04p03207

Spicher, A., Ilyasov, A. A., Miloch, W. J., Chernyshov, A. A., Clausen, L. B. N., Moen, J. I., . . . Saito, Y. (2016). Reverse flow events and small-scale effects in the cusp ionosphere. *Journal of Geophysical Research-Space Physics, 121*(10), 10466-10480. doi:10.1002/2016ja022999

Takeuchi, T., Araki, T., Viljanen, A., & Watermann, J. (2002a). Geomagnetic negative sudden impulses: Interplanetary causes and polarization distribution. *Journal of Geophysical Research: Space Physics, 107*(A7), SMP 7-1-SMP 7-14. doi:https://doi.org/10.1029/2001JA900152

Takeuchi, T., Araki, T., Viljanen, A., & Watermann, J. (2002b). Geomagnetic negative sudden impulses: Interplanetary causes and polarization distribution. *Journal of Geophysical Research-Space Physics, 107*(A7). doi:10.1029/2001ja900152

Valladares, C. E., Alcaydé, D., Rodriguez, J. V., Ruohoniemi, J. M., & Van Eyken, A. P. (1999). Observations of plasma density structures in association with the passage of traveling convection vortices and the occurrence of large plasma jets. *Ann. Geophys., 17*(8), 1020-1039. doi:10.1007/s00585-999-1020-6

Wannberg, G., Wolf, I., Vanhainen, L. G., Koskenniemi, K., Rottger, J., Postila, M., . . . Huuskonen, A. (1997). The EISCAT Svalbard radar: A case study in modern incoherent scatter radar system design. *Radio Science, 32*(6), 2283-2307. doi:Doi 10.1029/97rs01803

Zhao, H. Y., Shen, X. C., Tang, B. B., Tian, A. M., Shi, Q. Q., Weygand, J. M., . . . Pu, Z. Y. (2016). Magnetospheric vortices and their global effect after a solar wind dynamic pressure decrease. *Journal of Geophysical Research-Space Physics, 121*(2), 1071-1077. doi:10.1002/2015ja021646

Zhao, H. Y., Zhou, X. Z., Zong, Q. G., Weygand, J. M., Shi, Q. Q., Liu, Y., . . . Tian, A. M. (2019). Small-Scale Aurora Associated With Magnetospheric Flow Vortices After a Solar Wind Dynamic Pressure Decrease. *Journal of Geophysical Research-Space Physics, 124*(5), 3303-3311. doi:10.1029/2018ja026234

Zhou, X. Y., Strangeway, R. J., Anderson, P. C., Sibeck, D. G., Tsurutani, B. T., Haerendel, G., . . . Arballo, J. K. (2003). Shock aurora: FAST and DMSP observations. *Journal of Geophysical Research-Space Physics, 108*(A4). doi:10.1029/2002ja009701

Zhou, X. Y., & Tsurutani, B. T. (1999). Rapid intensification and propagation of the dayside aurora: Large scale interplanetary pressure pulses (fast shocks). *Geophysical Research Letters, 26*(8), 1097-1100. doi:Doi 10.1029/1999gl900173

Zou, S., Ozturk, D., Varney, R., & Reimer, A. (2017). Effects of sudden commencement on the ionosphere: PFISR observations and global MHD simulation. *Geophysical Research Letters, 44*(7), 3047-3058. doi:https://doi.org/10.1002/2017GL072678

Ionospheric Flow Vortex Induced by the Sudden Decrease in the Solar Wind Dynamic Pressure

Yaqi Jin[1], Jøran Idar Moen[1,2], Andres Spicher[3], Jianjun Liu[4], Lasse B. N. Clausen[1], and Wojciech J. Miloch[1]

[1]Department of Physics, University of Oslo, Oslo, Norway

[2]University Centre in Svalbard, Longyearbyen, Norway

[3]Department of Physics and Technology, UIT the Arctic University of Norway, Tromsø, Norway

[4]SOA Key Laboratory for Polar Science, Polar Research Institute of China, Shanghai, China

Corresponding author: Yaqi Jin (yaqi.jin@fys.uio.no)

Key Points:

- An ionospheric flow vortex is likely triggered by the sudden decrease in the solar wind dynamic pressure
- The flow vortex caused a reduction of the electron density
- In the morning sector, the flow vortex is clockwise and associated with upward field-aligned current and downward electron precipitation

Abstract

Abrupt changes in the solar wind dynamic pressure can greatly affect the Earth's magnetosphere-ionosphere system. We present an ionospheric flow vortex in the morning side during the sudden decrease in the solar wind dynamic pressure. The flow vortex was clearly observed by both the Hankasalmi radar and the azimuthal scan mode of the European Incoherent Scatter (EISCAT) Svalbard Radar (ESR). The flow vortex was first seen in the eastern field of view (FOV) of the Hankasalmi radar, and then propagated poleward and westward into the FOV of the ESR. During the passage of the flow vortex, a gradual decrease of electron density was observed by the field-aligned ESR 42 m antenna. When the equatorward directed ionospheric flow reached the ESR site, weak and visible increases in the electron density and electron temperature were observed. This impact was likely caused by soft electron precipitation associated with the clockwise flow vortex and upward field-aligned current. The azimuthal scan mode of the ESR 32 m radar at low elevation angle (30°) allowed us to measure key ionospheric parameters over a larger area (6° in latitude and 120° in azimuthal angle). The latitudinal scan of the electron temperature was used to derive the equatorward auroral boundary, which shows that the flow vortex was located in the subauroral region. We further demonstrated that it is possible to study the weak increase of electron density by using GPS total electron content (TEC) data. A minor TEC increase was observed near the center of the flow vortex.

1 Introduction

The Earth's magnetosphere-ionosphere system can be greatly affected by abrupt changes in the solar wind dynamic pressure. For example, the sudden increase in the solar wind dynamic pressure associated with a fast interplanetary shock can cause significant compression of the magnetosphere. Consequently, a positive geomagnetic sudden impulse (SI+) can be observed using ground-based magnetometers (e.g., Araki, 1994). Several phenomena can result from the compression of the magnetosphere. For example, the intensification of auroral luminosity can be found first near local noon, and then the intensification propagates to the nightside along the dawn and dusk flanks of the auroral oval (Zhou & Tsurutani, 1999; Zhou et al., 2003; Meurant et al., 2003). The sudden increase of the solar wind dynamic pressure can also induce travelling convection vortices (TCVs), which are east-west aligned pairs of oppositely-directed flow vortices (Friis-Christensen et al., 1988). Once generated, the TCVs propagate tailward away from local noon in the high-latitude ionosphere with a speed of several km/s (Friis-Christensen et al., 1988; Glassmeier et al., 1989; Lühr et al., 1996). The ionospheric flow vortices associated with TCVs have been observed by incoherent scatter radars (Lühr et al., 1996; Valladares et al., 1999) and Super Dual Auroral Radar Network (SuperDARN) radars (Lyatsky et al., 1999; Kataoka et al., 2003; Liu et al., 2011).

Though there exist many studies on the ionospheric effect due to the sudden solar wind pressure increase in the literature (Zou et al., 2017; Schunk et al., 1994; Collis & Haggstrom, 1991), studies on the impact of negative solar wind pressure pulses and magnetosphere expansion are quite rare. Early studies focused on the magnetic field perburbations related to the dynamic pressure decrease (Araki & Nagano, 1988; Takeuchi et al., 2002a). More recently, by using the SuperDARN King Salmon radar, Hori et al. (2012) reported poleward propagating vortex-like flow structures in the evening sector (~19 magnetic local time (MLT)) which were induced by a negative sudden impulse of the solar wind pressure. In another study, Zhao et al. (2016) reported a magnetospheric flow vortex that was driven by a negative solar wind dynamic pressure pulse. It has been found that the direction of the flow vortex was opposite to the scenario due to positive solar wind pressure pulses. By using the ground-based all-sky imager, the enhancement of the auroral luminosity has been found in the dawnside (~5 MLT) ionosphere in associated with an upward field-aligned current (FAC) (Zhao et al., 2019).

Besides the sudden changes in the solar wind dynamic pressure, another important mechanism that transfers momentum and energy to the magnetosphere-ionosphere system is magnetic reconnection (Dungey, 1961). The flux transfer event (FTE) is used to describe the transient, pulsed reconnection at the dayside magnetopause (Haerendel et al., 1978; Russell & Elphic, 1978, 1979; Lockwood & Hapgood, 1998). Southwood (1987) proposed a model to explain the ionospheric signatures of FTEs. In the Southwood model, a pair of field-aligned currents (FACs) with opposite direction is generated on the

poleward and equatorward edge of the newly reconnected flux tube. The pair of FACs sets up a twin vortex flow pattern on both sides of the newly reconnected flux tube. Later, by using the fast azimuth sweeps of the EISCAT Svalbard radar (ESR), Rinne et al. (2007) found that the return flow of the newly reconnected flux never formed simultaneously in pairs. As a result, an asymmetric version of the Southwood FTE model was proposed, where the return flow only occurs on the poleward side of the newly reconnected flux tube and this was termed as reversed flow event (RFE) (Rinne et al., 2007; Moen et al., 2008).

In this study, we report an event of ionospheric flow vortex in the morning side ionosphere. As will be shown later, this event is likely driven by an abrupt, step function like decrease in the solar wind dynamic pressure. The used instruments and datasets are introduced in section 2. Section 3 presents the event in detail, following by a summary and discussion in section 4.

2 Instrumentation and dataset

In this study, we use the European Incoherent Scatter (EISCAT) Svalbard Radar (ESR) in Longyearbyen, the SuperDARN radar in Hankasalmi, Finland, and Global Positioning System (GPS) receiver in Ny-Ålesund.

The ESR in Longyearbyen (78.15°N, 16.02°E; magnetic latitude (MLAT) 75.43°N) consists of a 32-m steerable antenna and a 42-m static field-aligned antenna (azimuth = 182.1°, elevation = 81.6°). The basic ionospheric properties such as the electron density (Ne), electron temperature (Te), ion temperature (Ti), and line-of-sight ion velocity (Vi) can be obtained from both antennas (e.g., Wannberg et al., 1997). On 3 December 2011, the ESR 32 m antenna was operated in a fast azimuth scan mode from 6:30 to 8:30 UT to study the RFEs (Carlson et al., 2002; Rinne et al., 2007). The 32-m antenna beam moved between azimuth angles of 180° and 300° at an elevation angle of 30° and was alternating between clockwise and anticlockwise motion. With the highest allowed azimuthal scan speed of 0.625°/s, the radar beam completes one 120° azimuthal scan in 192 s. The selected pulse code *taro* allows for simultaneous transmission and receiving of signals by both antennas. The stored data resolution is 6.4 s, which results in 30 adjacent radar beam directions in one complete azimuthal scan. For the data from the ESR 42 m antenna, the data are analyzed using GUISDAP with integration time of 64 s.

For the ionospheric drift velocities, we use the data from the coherent scatter high frequency (HF) radar in Hankasalmi (62.3°N, 26.6°E) from SuperDARN (Milan et al., 1999; Greenwald et al., 1995). The HF radar operates in 16 azimuthal beams that are separated by about 3.2°. By analyzing the backscatter echoes from field-aligned ionospheric irregularities, the line-of-sight Doppler drift velocity, spectral

width, and power can be obtained. We use the SuperDARN data at the FITACF level, which is a commonly used routine to process SuperDARN auto-correlation functions (see e.g., Ribeiro et al., 2013).

The solar wind data from the OMNI database are used to present the upstream solar wind conditions (King & Papitashvili, 2005). The OMNI interplanetary magnetic field (IMF) is presented in the geocentric solar magnetospheric coordinates. The Sym-H index and AE indices in 1-min resolution is used to show the global magnetic response to the solar wind variations. The Sym-H and AE indices were obtained from the World Data Center for Geomagnetism at Kyoto University (http://wdc.kugi.kyoto-u.ac.jp/).

The GPS data in Ny-Ålesund (78.9°N, 11.9°E) is taken from the International Global Navigation Satellite System (GNSS) Service. The Receiver Independent Exchange Format (RINEX) format data in 1-s resolution is downloaded from the high-rate data of NASA's Crustal Dynamics Data Information System (CDDIS) https://cddis.nasa.gov/archive/gnss/data/highrate/. The carrier phase observations at L1 and L2 bands are used to calculate the total electron content (TEC). In this study, we only use 1-s resolution TEC data from GPS satellite 31.

3 Results

The event was observed on December 3, 2011 during the EISCAT campaign for the Norwegian sounding ICI-3 rocket (Spicher et al., 2016; Jin et al., 2017; Jin et al., 2019). Figures 1a-c present the upstream solar wind and IMF information from the OMNI dataset. The solar wind density (Figure 1a) decreased abruptly from 13 cm^{-3} at 6:39 UT to 3 cm^{-3} at 6:42 UT. This resulted in a sharp decrease in the solar wind dynamic pressure (P_{dyn}) from 4.9 nPa to slightly below 1 nPa (Figure 1b). The IMF was characterized by a sharp southward turn from 6:37 UT to 6:41 UT. The IMF By remained negative with decreasing magnitude. The AU, AL and AE indices are shown in Figure 1d. The AL index was relatively stable, while AE and AU slightly increased from ~6:39 UT. The Kp index was stable at 2+, while the Sym-H index decreased quickly from 6:39 UT. The decrease of the Sym-H index was a response of the decrease of solar wind dynamic pressure and a decrease of the magnetopause current (Takeuchi et al., 2002b). We therefore consider 6:39 UT as the time when the solar wind pressure decrease arrived at the dayside magnetosphere.

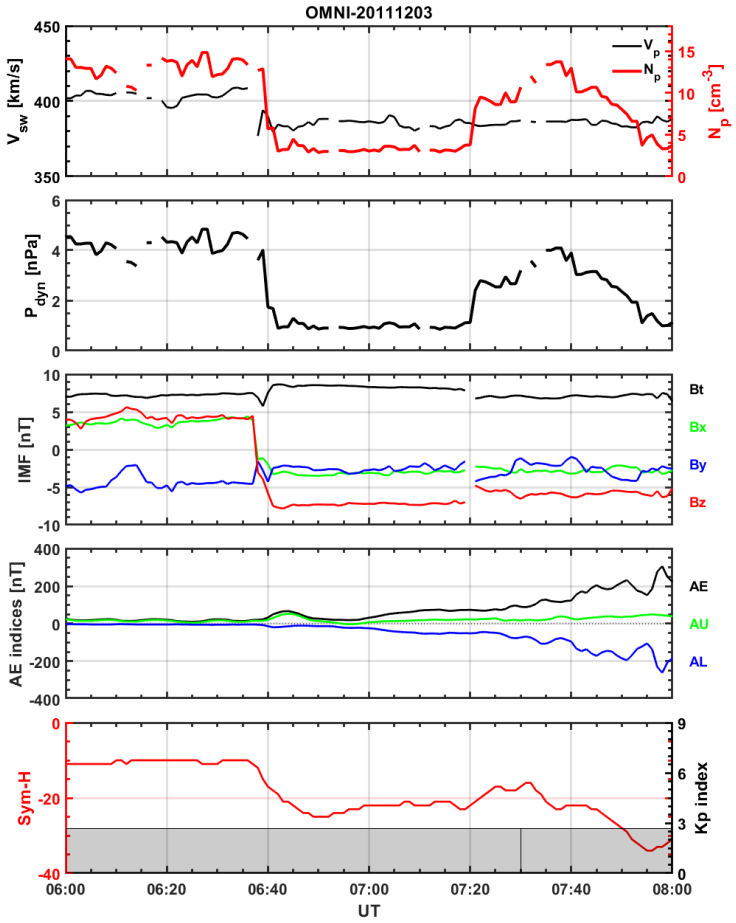

Figure 1. An overview of the solar wind, IMF, AE, Sym-H, and Kp indices from 6:00 to 8:00 UT on 3 December 2011. (a) The solar wind velocity (black) and proton density (Np, red); (b) the solar wind dynamic pressure; (c) the IMF strength (Bt, black), By (blue), and Bz (red) components; (d) AU (green), AL (blue), and AE (black) indices; (e) the Sym-H (red) and Kp (black shaded) indices. IMF = Interplanetary Magnetic Field.

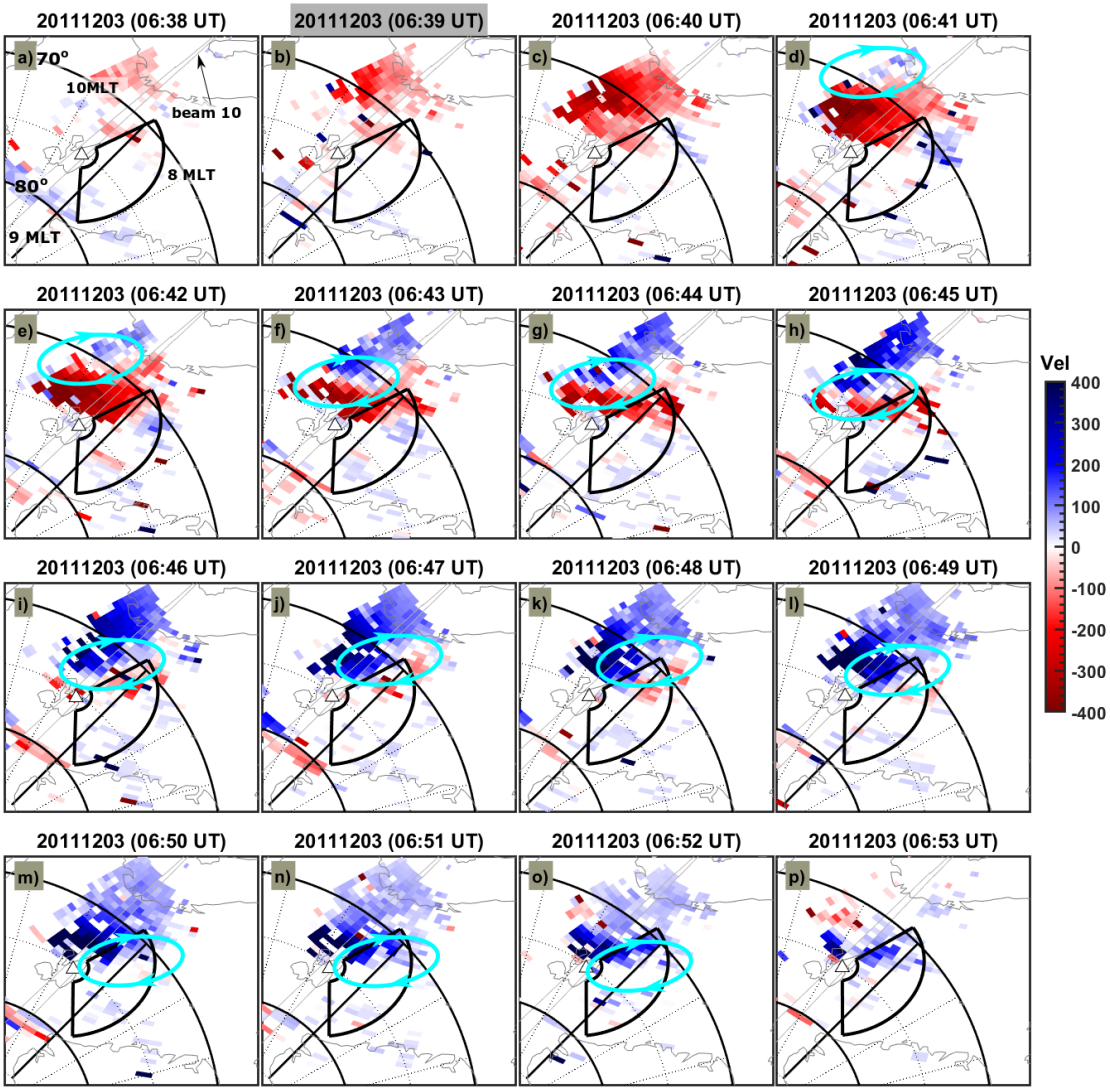

Figure 2. The Doppler drift velocity observed in the field-of-view of the Hankasalmi HF radar with the time cadence of 1 min. The data is presented in MLAT/MLT coordinates, with magnetic noon to the top an dawn to the right. In each panel, the radar beam 10 is marked. The black fan-shaped area is the field-of-view of the ESR 32 m antenna. The white triangle is the location of ESR in Longyearbyen. The enhanced poleward ionospheric flow was first visible at 06:39 UT.

Figure 2 shows the Doppler drift velocity in the field-of-view (FOV) of the Hankasalmi HF radar. The radar FOV was located in the morning sector (8-10 MLT). The enhanced poleward (red) ionospheric flow was first observed in the eastern side of the FOV around 68° MLAT and 10 MLT (Figure 2b). Then the enhanced flow moved poleward and tailward toward earlier MLT. The first equatorward directed flow was observed at 6:41 UT (Figure 2d). This was a clockwise flow vortex as annotated by the arrowed cyan ellipse. The whole vortex flow moved westward and entered the FOV of the scan mode of the ESR 32 m antenna (as indicated by the black fan-shaped area on the westside of Svalbard. The data from ESR 42 m

beam (field-aligned in the F region, azimuth 182.1°, elevation 81.6°) is also available. The ESR radar site is annotated by a white triangle in each panel of Figure 2.

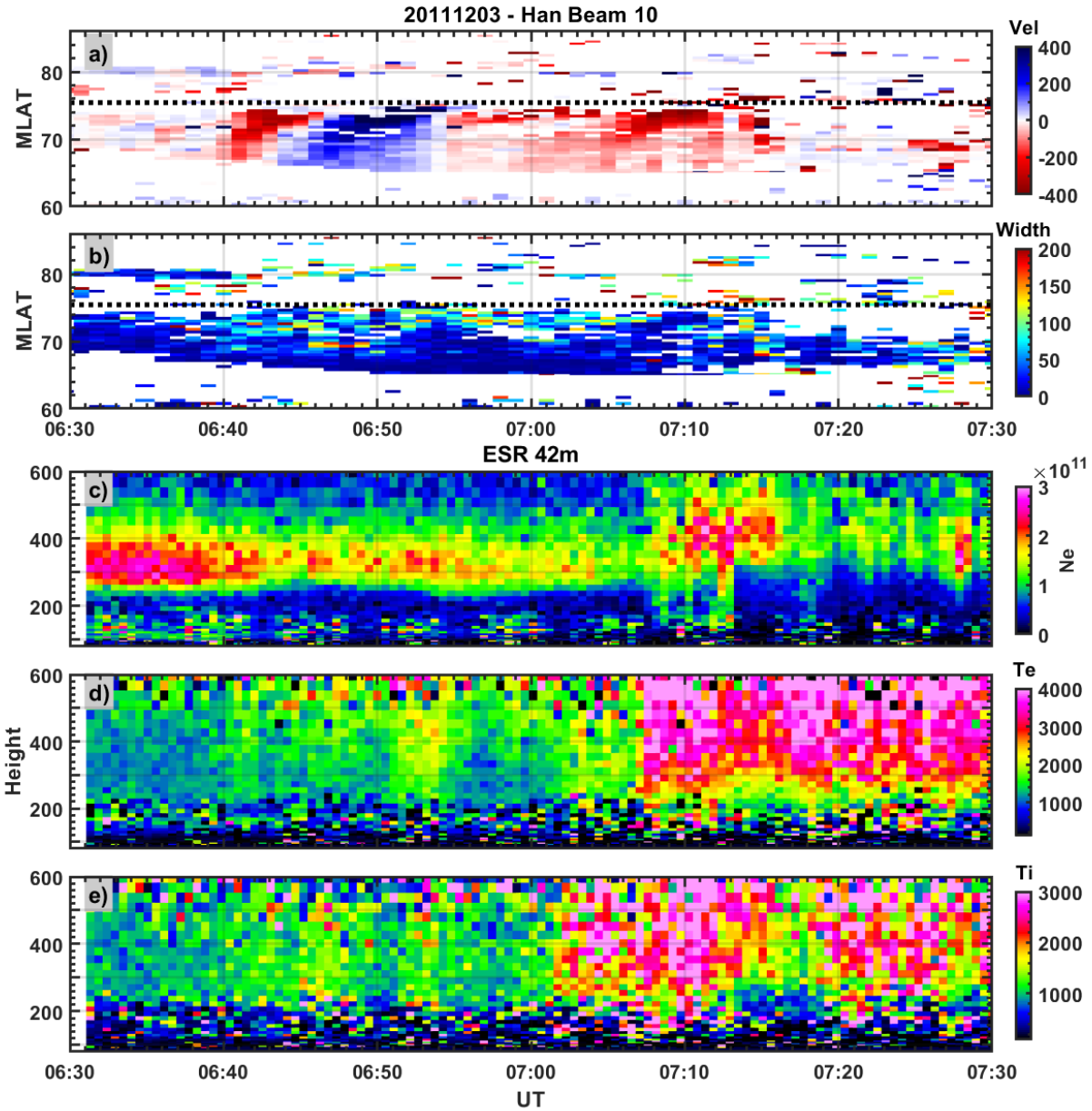

Figure 3. Ionospheric data from the Hankasalmi HF radar and the EISCAT 42 m antenna. The Doppler drift velocity (a) and spectral width (b) from beam 10 of the Hankasalmi HF radar as a function of magnetic latitude (MLAT). The black horizontal dashed line shows the location of the ESR 42 m radar at 75.43° MLAT. The altitude profiles of electron density (c), electron temperature (d), ion temperature (e) from the field-aligned 42 m antenna.

The radar beam 10 of the Hankasalmi radar is aligned with ESR (Figure 2a). The range-time plot of data from beam 10 is presented in Figures 3a-3b, where the black dashed horizontal line shows the location of

the ESR site. Figure 3a shows that the poleward directed ionospheric flow reached ESR around 6:45 UT, while the equatorward directed flow reached the ESR site around 6:52 UT. Note that there is a lack of HF backscatter around the ESR site, which could be due to not optimal propagation ray-path of the radar signal. Figure 3b shows the spectral width from beam 10, which shows that the flow vortex was associated with slightly enhanced spectral width. We present the ionospheric data from the ESR 42 m radar in Figures 3c-3e. The electron density profile shows a region of moderate high electron density ($2.5\times10^{11}m^{-3}$) at ~250-400 km between 6:30-6:40 UT. When the flow vortex reached near the ESR site, the electron density significantly decreased to around $1.5\times10^{11}m^{-3}$. Interestingly, there was a region of slightly increase in electron density around 6:51-6:53 UT. This was at the same time when the equatorward directed flow (blue) reached the ESR site (Figure 3a). The minor increase of the electron density was also associated with the slight increase in the electron temperature. As will be discussed later, this was likely associated with an auroral arc in connection to the flow vortex (Lühr et al., 1996). We also observed weak by identifiable ion temperature associated with the flow vortex. This was likely due to the impact of enhanced ion frictional heating during enhanced ionospheric flow. We note that the ESR 42 m antenna was equatorward of the main auroral oval when the flow vortex is observed (cf. Figure 5). As the IMF Bz turned southward, the main auroral oval expanded equatorward. The main auroral oval should arrive at the ESR site at about 7:07 UT as indicated by the abrupt increase in the electron temperature (Figure 3d). The ongoing soft precipitation also caused enhanced electron density and ion temperature.

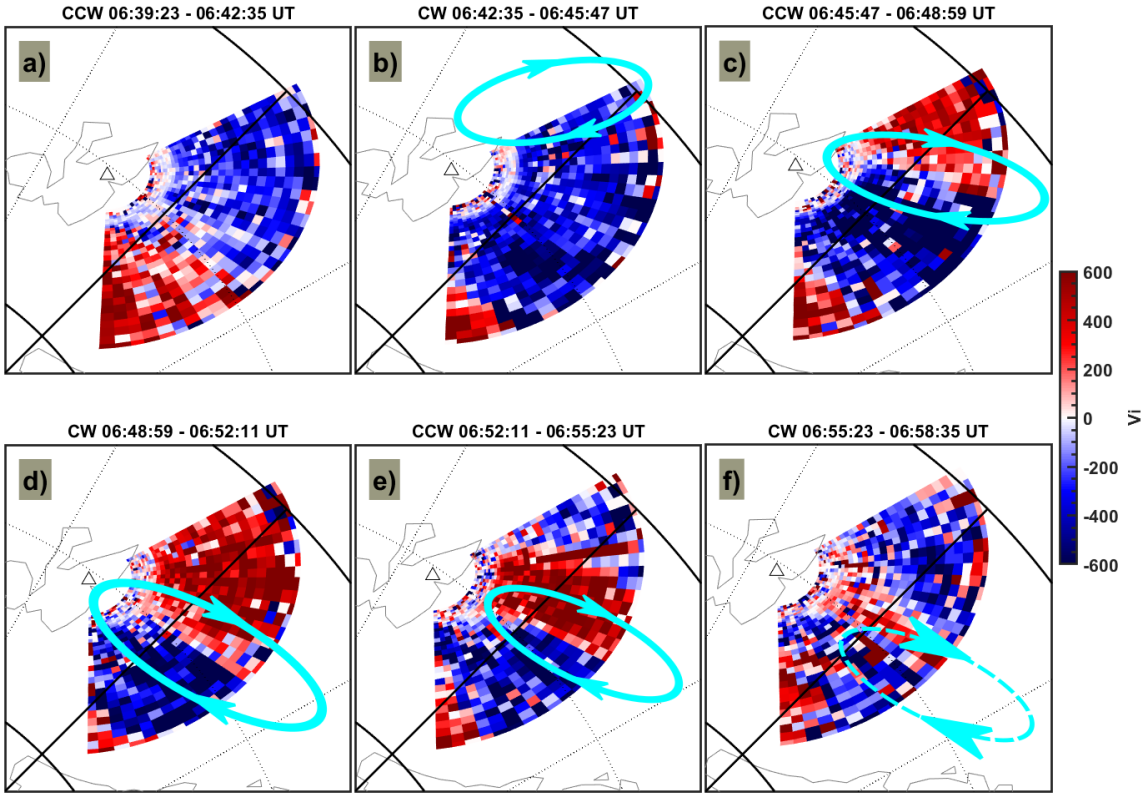

Figure 4. Line-of-sight ion velocity (Vi) observed by the ESR 32 m antenna. Positive (red) velocities are away from the radar site. The scan time is shown on the top of each panel, where "cw" is clockwise and "ccw" is counterclockwise scan. The arrowed cyan ellipse indicates the flow vortex.

The ESR 32 m radar was operating in a fast azimuthal scan mode at an elevation of 30° during this event. Figure 4 shows the ion velocity in 6 azimuthal scans, which show the evolution of the flow vortex when it entered and left the FOV of ESR. Figure 4a shows the scan before the flow vortex entered the FOV of ESR. Figure 4b shows that the poleward directed flow first entered the southern part of the ESR FOV as indicated by the toward (blue) ion velocity. The inferred flow vortex is overlaid as an arrowed cyan ellipse in each panel. The equatorward directed flow entered the FOV in Figure 4c as indicated by away (red) ion velocity from the ESR 32 m radar. The vortex flow continued moving westward and it was barely visible during the scan time in Figure 4f. The flow shear between the positive and negative ion velocity was evidently visible in Figures 4c-4e.

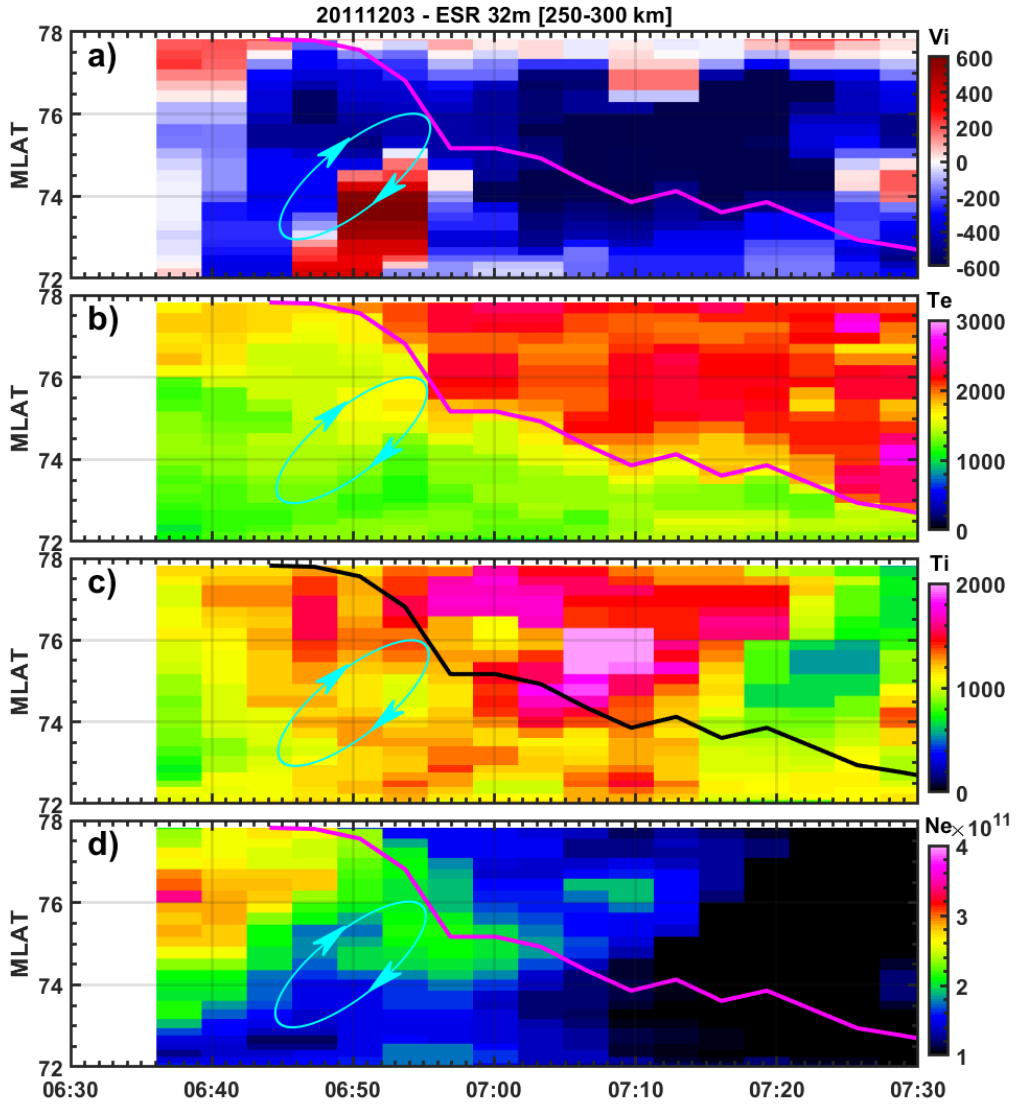

Figure 5. The ionospheric parameters obtained from the ESR 32 m antenna by averaging the data from altitudes between 250 – 300 km. Line-of-sight ion velocity (a), electron temperature (b), ion temperature (c), and electron density (d). In each panel, the magenta (black in panel c) line marks the equatorward auroral boundary as derived from the electron temperature data by selecting the equatorward boundary at Te = 1800 K. The arrowed cyan ellipse indicates the flow vortex.

It is also possible to obtain other plasma parameters from the scan mode of the ESR 32 m antenna. Figure 5 shows the ionospheric parameters from the ESR 32 m antenna, which were averaged over altitudes 250-300 km. The data were scanned along fixed range gates and are presented as a function of MLAT. As one azimuthal scan takes 192 s, the time resolution is 192 s in the horizontal axis. The flow vortex can be seen from the ion velocity from blue (toward) near 6:42 UT and red (toward) near 6:50 UT. The flow vortex is annotated by the arrowed cyan ellipse in Figure 5. Note that the measured ion velocity is line-of-sight

velocity along the radar beam, i.e., it was mainly in the north-south direction below about 74° MLAT, and it became more aligned in the east-west direction above 74° MLAT (cf. Figure 4). Figure 5b shows the electron temperature data. The latitudinal profile of electron temperature can be used to identify the auroral boundary (Doe et al., 2001). The equatorward auroral boundary was obtained by selecting the most equatorward electron temperature that exceeded 1800 K. The derived auroral boundary is plotted as a magenta line in Figures 5a-5b. The auroral boundary shifted equatorward as a response to the southward turning of the IMF Bz. The equatorward auroral boundary reached 74.3° MLAT (ESR site) at around 7:07 UT. This was consistent with the sudden increase of the electron temperature as measured by the ESR 42 m antenna around the same time (Figure 3d). This justifies that the derived equatorward auroral boundary from the electron temperature data is valid. Notice that the flow vortex was equatorward of the equatorward auroral boundary when it was observed in the FOV of the ESR 32 m antenna. Figure 5c displays the ion temperature, which shows moderate enhanced Ti in association with the flow vortex. However, the strongest ion temperature enhancement occurred in the auroral zone when there was a strong eastward flow near 75° MLAT around 7:10 UT. The averaged electron density between 250-300 km in Figure 5d shows a gradual decrease of electron density that was similar to the ESR 42 m data. Interesting, there was a weak increase of the electron density when the flow vortex was observed, and this coincided with a slight increase of the electron temperature (cf. Figure 4b).

4. Summary and Discussion

In this study, we have presented an event of ionospheric flow vortex that was triggered by a sudden decrease of the solar wind dynamic pressure. The flow vortex was observed in the morning sector (8-10 MLT and 65°-75° MLAT). The 2-D morphology of the flow vortex was clearly observed by both the Hankasalmi coherent scatter HF radar and the azimuthal scan mode of the ESR 32 m radar. The flow vortex was first seen in the eastern FOV of the HF radar, and then it propagated poleward and westward into the FOV of the ESR. When the flow vortex arrived near the ESR site, a gradual decrease of the electron density was observed by the field-aligned 42 m radar. When the equatorward directed ionospheric flow reached the ESR site, weak and visible increases in the electron density and electron temperature were observed. This impact was likely caused by soft electron precipitation associated with the flow vortex (Lühr et al., 1996; Doe et al., 2001). The azimuthal scan mode of the ESR 32 m radar at low elevation angle (30°) allowed us to measure key ionospheric parameters over a larger area (6° in MLAT and 120° in azimuthal angle). Velocity shear associated with the flow vortex was clearly visible in 3 scans (3×192 s = 9.6 min). The latitudinal scan of the electron temperature at 250-300 km was obtained in order to derive the equatorward auroral boundary. Apparently, the flow vortex was located in the subauroral region in the morning sector (cf. Figure 5). This is consistent with the studies of magnetic

signature of TCVs, i.e., the TCV center is located in the closed field line within the region of plasmasheet (Moretto & Yahnin, 1998).

As it often happens, the sudden decrease of the solar wind dynamic pressure occurred in association with the orientation change of the IMF, i.e., the sudden decrease in the solar wind dynamics pressure was associated with a southward turning of the IMF Bz. However, we can rule out the contribution of the southward turning of the IMF due to two reasons: 1) the flow vortex occurred equatorward of the auroral boundary, and it originated at lower latitudes and moved poleward and westward; while the FTE induced flow occurs near the open/closed field line boundary and propogates poleward; 2) the FTE driven flow is poleward during negative Bz (Southwood, 1987; Cowley & Lockwood, 1992), and this contradicts with the equatorward directed flow in the flow vortex. Note that this is also different from the reversed flow event (RFE) in the cusp ionosphere (Rinne et al., 2007; Moen et al., 2008; Jin et al., 2019). The RFE is interpreted as the return flow on the poleward side of the newly reconnected flux tube in the cusp region (see Figure 7 in Jin et al., 2019). On the contrary, the equatorward return flow of the flow vortex occurred on the equatorward side in our event. In addition, the reversed flow event occurs in the open field line region, while the present event occurred in closed field line. Actually, a series of reversed flow events were indeed observed in the cusp ionosphere later this day (see e.g., Jin et al., 2019), but they were not related to the event in this study.

There are a few studies that focused on the impact on the ionospheric response to SI+ and TCV. For example, Kataoka et al. (2003) observed transient production of F-region irregularities during the passage of TCV. Valladares et al. (1999) observed electron density depletion by a factor of two associated with a TCV event. The decreased electron density was explained by the fast ionospheric flow and ion frictional heating with subsequent increased recombination rate. In our event, we also observed a decrease of electron density (from 2.5×10^{11} m^{-3} to 1.5×10^{11} m^{-3}) during the passage of the flow vortex. The ion temperature was also enhanced. This indicates that the decrease of electron density should be related to fast fows, as suggested by Valladares et al. (1999) and Ogawa et al. (2001).

Unlike the impact of solar wind dynamic pressure increases, the impact of solar wind dynamic pressure decreases are relatively less studied in the literature. Zhao et al. (2016) observed magnetospheric flow vortex driven by a negative solar wind dynamic pressure pulse, where the observed vortex rotated in a direction opposite to the case due to positive solar wind dynamic pressure pulses. The negative solar wind pressure can induce FACs in the dawn and dusk sectors by Region 2 sense FACs, i.e., it flows out of (into) the ionosphere in the dawnside (duskside) (Zhao et al., 2016).

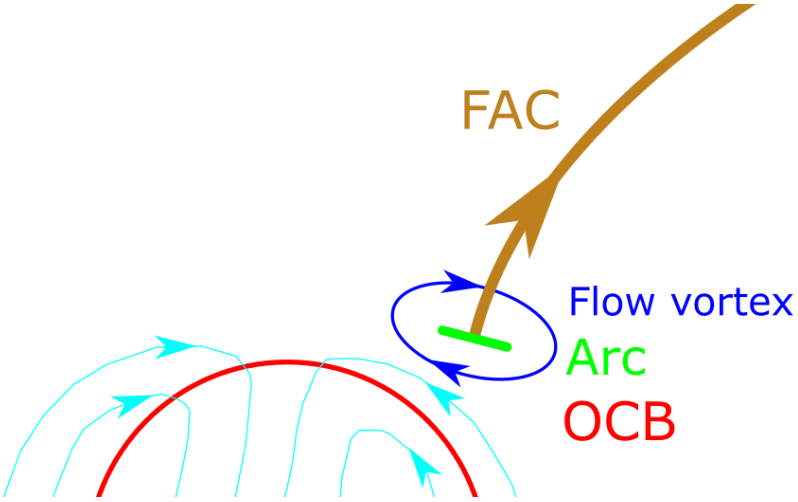

Figure 6. Sketmatics of the observation scenario. The observed clockwise ionospheric flow vortex is equatorward of the main auroral oval, and it is associated with an upward field aligned current (FAC) and downward electron precipitation. OCB = open/closed field line boundary.

Based on the previous literature and our observations, we summarize the observation scenario in Figure 6. The clockwise ionospheric flow vortex was observed in the morning side ionosphere and it was equatorward of the main auroral oval. Due to the fast flow (or flow shear) associated with the flow vortex, the electron density was significantly depleted within 10 min. The clockwise flow vortex was connected to the magnetosphere through an upward FAC, which was associated with an auroral arc due to accelerated electron precipitation. The soft precipitation caused weak enhancement of ionospheric density and electron temperature.

Given the observational feature in the ionosphere, this phenomenon should also be detectable by using ground-based GPS TEC data. For example, Jin et al. (2016) presented an event showing the global TEC response of the auroral ionosphere due to the sudden increase of the solar wind dynamic pressure associated with an interplanetary shock. The fast anti-sunward propagation of TEC enhancements due to shock-induced aurora was observed. Similarly, we show that it is also possible to detect the TEC response due to the solar wind pressure decrease by coordinated observations. Figures 7a-7b show the ion velocity, electron density and electron temperature during the azimuthal scan at 6:48:59-6:52:11 UT. The ionospheric parameters during other azimuthal scan time can be found in the supporting information. The pierce point of PRN31 tracked from Ny-Ålesund is shown as an asterisk, which was located near the flow shear during this scan. The pierce point is projected to an altitude of 300 km according to the electron density profile in Figure 3c. Figures 7b-7c show moderate electron density as well as noisy and enhanced electron temperature. Similar minor increase of the electron density and temperature can be also seen from Figures 3c-3d as well as Figures 5d and 5d. However, due to the noisiness of the ESR data, it is

difficult to conclude whether the electron density and temperature indeed increased near the flow shear. Figure 7d shows the 1-Hz resolution GPS TEC data from PRN31 (red) and its moving average (black) in a sliding window of 15 min. Clearly the TEC data shows gradual decrease from 6:40 UT onward. There was a minor increase in the TEC data from 6:48:30 UT to 6:52 UT. This was the time when PRN31 was located near the flow shear during the scan in Figures 7a-7c. The minor TEC increase (ΔTEC $\approx$ 1 TECu, where 1 TECu = 10^{16} electrons/m^2) was likely caused by auroral particle precipitation near the flow shear. This confirms that the weak increases in electron density and electron temperature by the ESR should be real. This also demonstrates that it should be possible to detect the ionospheric effect due to sudden solar wind dynamic pressure decrease by using the GPS TEC data. By using the global distributed networks of GPS receivers (Jin et al., 2016), one can investigate the propagation and evolution of the associated ionospheric effect. This provides another alternative dataset (in addition to magnetometers and optical auroral data) to study the response and evolution of the magnetosphere-ionosphere system due to the impact of the negative solar wind pressure pulse. Such studies will be explored in future investigations.

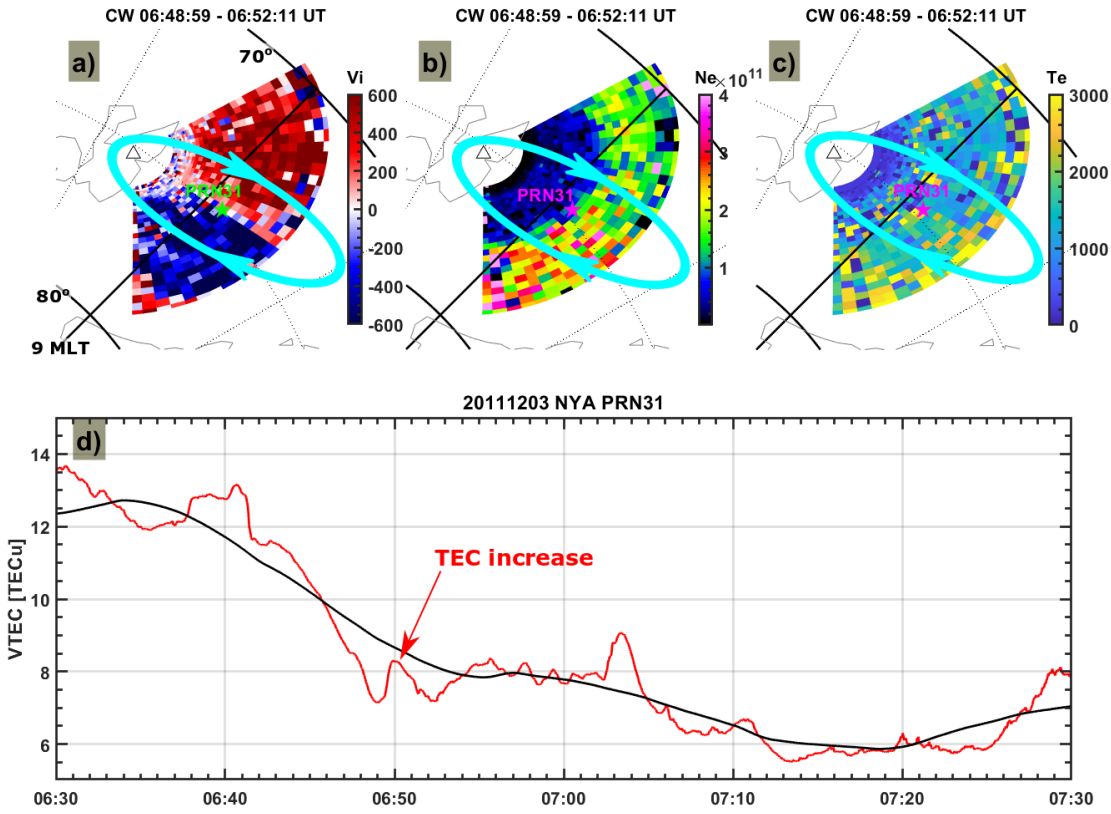

Figure 7. The observations from the ESR 32 m antenna and the vertical GPS TEC data from Ny-Ålesund (NYA). The line-of-sight ion velocity (a), electron density (b), and the electron temperature (c) from the scan of the ESR 32 m antenna. The pierce point of PRN31 at an altitude of 300 km is plotted as an

asterisk in each panel. (d) the 1-Hz resolution VTEC (red) and its moving average (black) from PRN31 tracked in Ny-Ålesund.

Acknowledgments

YJ and WJM acknowledge funding from the European Research Council (ERC) under the European Union's Horizon 2020 research and innovation programme (ERC Consolidator Grant agreement No. 866357, POLAR-4DSpace). This research is a part of the 4DSpace Strategic Research Initiative at the University of Oslo. AS acknowledges funding from the RCN grant 326039, and the UiT The Arctic University of Norway contribution to the EISCAT 3D (RCN funded grant 245683).

Open Research

The IMF and solar wind data are provided by the NASA OMNIWeb service (http://omniweb.gsfc.nasa.gov). EISCAT is an international association supported by research organizations in China (CRIRP), Finland (SA), Japan (NIPR and STEL), Norway (NFR), Sweden (VR), and the United Kingdom (NERC). Data from EISCAT can be obtained from the Madrigal database http://www.eiscat.se/madrigal. SuperDARN is a collection of radars funded by national scientific funding agencies of Australia, Canada, China, France, Japan, South Africa, United Kingdom, and the United States of America. The SuperDARN data can be obtained from http://vt.superdarn.org/tiki-index.php. The GPS data can be obtained through https://cddis.nasa.gov/archive/gnss/data/highrate/.

References

Araki, T. (1994). A Physical Model of the Geomagnetic Sudden Commencement. In *Solar Wind Sources of Magnetospheric Ultra-Low-Frequency Waves* (pp. 183-200).

Araki, T., & Nagano, H. (1988). Geomagnetic response to sudden expansions of the magnetosphere. *Journal of Geophysical Research: Space Physics, 93*(A5), 3983-3988. doi:https://doi.org/10.1029/JA093iA05p03983

Carlson, H. C., Oksavik, K., Moen, J., van Eyken, A. P., & Guio, P. (2002). ESR mapping of polar-cap patches in the dark cusp. *Geophysical Research Letters, 29*(10). doi:10.1029/2001gl014087

Collis, P. N., & Haggstrom, I. (1991). HIGH-LATITUDE IONOSPHERIC RESPONSE TO A GEOMAGNETIC SUDDEN COMMENCEMENT. *Journal of Atmospheric and Terrestrial Physics, 53*(3-4), 241-248. doi:10.1016/0021-9169(91)90108-j

Cowley, S. W. H., & Lockwood, M. (1992). Excitation and Decay of Solar Wind-Driven Flows in the Magnetosphere-Ionosphere System. *Annales Geophysicae-Atmospheres Hydrospheres and Space Sciences, 10*(1-2), 103-115. Retrieved from <Go to ISI>://WOS:A1992HL02700010

Doe, R. A., Kelly, J. D., & Sanchez, E. R. (2001). Observations of persistent dayside F region electron temperature enhancements associated with soft magnetosheathlike precipitation. *Journal of Geophysical Research-Space Physics, 106*(A3), 3615-3630. doi:Doi 10.1029/2000ja000186

Dungey, J. W. (1961). Interplanetary Magnetic Field and Auroral Zones. *Physical Review Letters, 6*(2), 47-&. doi:DOI 10.1103/PhysRevLett.6.47

Friis-Christensen, E., McHenry, M., Clauer, C., & Vennerstrøm, S. (1988). Ionospheric traveling convection vortices observed near the polar cleft: A triggered response to sudden changes in the solar wind. *Geophysical Research Letters, 15*(3), 253-256. doi:10.1029/GL015i003p00253

Glassmeier, K.-H., Hönisch, M., & Untiedt, J. (1989). Ground-based and satellite observations of traveling magnetospheric convection twin vortices. *Journal of Geophysical Research: Space Physics, 94*(A3), 2520-2528. doi:https://doi.org/10.1029/JA094iA03p02520

Greenwald, R. A., Baker, K. B., Dudeney, J. R., Pinnock, M., Jones, T. B., Thomas, E. C., . . . Yamagishi, H. (1995). Darn Superdarn - a Global View of the Dynamics of High-Latitude Convection. *Space Science Reviews, 71*(1-4), 761-796. doi:Doi 10.1007/Bf00751350

Haerendel, G., Paschmann, G., Sckopke, N., Rosenbauer, H., & Hedgecock, P. C. (1978). Frontside boundary-layer of magnetosphere and problem of reconnection. *Journal of Geophysical Research-Space Physics, 83*(NA7), 3195-3216. doi:10.1029/JA083iA07p03195

Hori, T., Shinbori, A., Nishitani, N., Kikuchi, T., Fujita, S., Nagatsuma, T., . . . Seki, K. (2012). Evolution of negative SI-induced ionospheric flows observed by SuperDARN King Salmon HF radar. *Journal of Geophysical Research-Space Physics, 117*. doi:10.1029/2012ja018093

Jin, Y., Moen, J. I., Spicher, A., Oksavik, K., Miloch, W. J., Clausen, L. B. N., . . . Saito, Y. (2019). Simultaneous Rocket and Scintillation Observations of Plasma Irregularities Associated With a Reversed Flow Event in the Cusp Ionosphere. *Journal of Geophysical Research: Space Physics, 124*(8), 7098-7111. doi:10.1029/2019ja026942

Jin, Y. Q., Moen, J. I., Oksavik, K., Spicher, A., Clausen, L. B. N., & Miloch, W. J. (2017). GPS scintillations associated with cusp dynamics and polar cap patches. *Journal of Space Weather and Space Climate, 7*. doi:10.1051/swsc/2017022

Jin, Y. Q., Zhou, X. Y., Moen, J. I., & Hairston, M. (2016). The auroral ionosphere TEC response to an interplanetary shock. *Geophysical Research Letters, 43*(5), 1810-1818. doi:10.1002/2016gl067766

Kataoka, R., Fukunishi, H., Hosokawa, K., Fujiwara, H., Yukimatu, A. S., Sato, N., & Tung, Y. K. (2003). Transient production of F-region irregularities associated with TCV passage. *Annales Geophysicae, 21*(7), 1531-1541. doi:10.5194/angeo-21-1531-2003

King, J. H., & Papitashvili, N. E. (2005). Solar wind spatial scales in and comparisons of hourly Wind and ACE plasma and magnetic field data. *Journal of Geophysical Research-Space Physics, 110*(A2). doi:10.1029/2004ja010649

Liu, J. J., Hu, H. Q., Han, D. S., Araki, T., Hu, Z. J., Zhang, Q. H., . . . Ebihara, Y. (2011). Decrease of auroral intensity associated with reversal of plasma convection in response to an interplanetary shock as observed over Zhongshan station in Antarctica. *Journal of Geophysical Research: Space Physics, 116*(A3). doi:https://doi.org/10.1029/2010JA016156

Lockwood, M., & Hapgood, M. A. (1998). On the cause of a magnetospheric flux transfer event. *Journal of Geophysical Research-Space Physics, 103*(A11), 26453-26478. doi:10.1029/98ja02244

Lyatsky, W. B., Sofko, G. J., Kustov, A. V., Andre, D., Hughes, W. J., & Murr, D. (1999). Traveling convection vortices as seen by the SuperDARN HF radars. *Journal of Geophysical Research-Space Physics, 104*(A2), 2591-2601. doi:10.1029/1998ja900007

Lühr, H., Lockwood, M., Sandholt, P. E., Hansen, T. L., & Moretto, T. (1996). Multi-instrument ground-based observations of a travelling convection vortices event. *Annales Geophysicae-Atmospheres Hydrospheres and Space Sciences, 14*(2), 162-181. doi:DOI 10.1007/s00585-996-0162-z

Meurant, M., Gérard, J.-C., Hubert, B., Coumans, V., Blockx, C., Østgaard, N., & Mende, S. B. (2003). Dynamics of global scale electron and proton precipitation induced by a solar wind pressure pulse. *Geophysical Research Letters, 30*(20). doi:https://doi.org/10.1029/2003GL018017

Milan, S. E., Davies, J. A., & Lester, M. (1999). Coherent HF radar backscatter characteristics associated with auroral forms identified by incoherent radar techniques: A comparison of CUTLASS and EISCAT observations. *Journal of Geophysical Research-Space Physics, 104*(A10), 22591-22604. doi:Doi 10.1029/1999ja900277

Moen, J., Rinne, Y., Carlson, H. C., Oksavik, K., Fujii, R., & Opgenoorth, H. (2008). On the relationship between thin Birkeland current arcs and reversed flow channels in the winter cusp/cleft ionosphere. *Journal of Geophysical Research-Space Physics, 113*(A9). doi:10.1029/2008ja013061

Moretto, T., & Yahnin, A. (1998). *Mapping travelling convection vortex events with respect to energetic particle boundaries.* Annales Geophysicae, pp. 891-899.

Ogawa, T., Buchert, S. C., Nishitani, N., Sato, N., & Lester, M. (2001). Plasma density suppression process around the cusp revealed by simultaneous CUTLASS and EISCAT Svalbard radar observations. *Journal of Geophysical Research-Space Physics, 106*(A4), 5551-5564. doi:Doi 10.1029/2000ja900111

Ribeiro, A. J., Ruohoniemi, J. M., Ponomarenko, P. V., N. Clausen, L. B., H. Baker, J. B., Greenwald, R. A., . . . de Larquier, S. (2013). A comparison of SuperDARN ACF fitting methods. *Radio Science, 48*(3), 274-282. doi:https://doi.org/10.1002/rds.20031

Rinne, Y., Moen, J., Oksavik, K., & Carlson, H. C. (2007). Reversed flow events in the winter cusp ionosphere observed by the European Incoherent Scatter (EISCAT) Svalbard radar. *Journal of Geophysical Research-Space Physics, 112*(A10). doi:10.1029/2007ja012366

Russell, C. T., & Elphic, R. C. (1978). Initial ISEE magnetometer results - magnetopause observations. *Space Science Reviews, 22*(6), 681-715. Retrieved from <Go to ISI>://WOS:A1978GM11300002

Russell, C. T., & Elphic, R. C. (1979). ISEE observations of flux-transfer events at the dayside magnetopause *Geophysical Research Letters, 6*(1), 33-36. doi:10.1029/GL006i001p00033

Schunk, R. W., Zhu, L., & Sojka, J. J. (1994). Ionospheric response to traveling convection twin vortices. *Geophysical Research Letters, 21*(17), 1759-1762. doi:https://doi.org/10.1029/94GL01059

Southwood, D. J. (1987). The Ionospheric Signature of Flux-Transfer Events. *Journal of Geophysical Research-Space Physics, 92*(A4), 3207-3213. doi:DOI 10.1029/JA092iA04p03207

Spicher, A., Ilyasov, A. A., Miloch, W. J., Chernyshov, A. A., Clausen, L. B. N., Moen, J. I., . . . Saito, Y. (2016). Reverse flow events and small-scale effects in the cusp ionosphere. *Journal of Geophysical Research-Space Physics, 121*(10), 10466-10480. doi:10.1002/2016ja022999

Takeuchi, T., Araki, T., Viljanen, A., & Watermann, J. (2002a). Geomagnetic negative sudden impulses: Interplanetary causes and polarization distribution. *Journal of Geophysical Research: Space Physics, 107*(A7), SMP 7-1-SMP 7-14. doi:https://doi.org/10.1029/2001JA900152

Takeuchi, T., Araki, T., Viljanen, A., & Watermann, J. (2002b). Geomagnetic negative sudden impulses: Interplanetary causes and polarization distribution. *Journal of Geophysical Research-Space Physics, 107*(A7). doi:10.1029/2001ja900152

Valladares, C. E., Alcaydé, D., Rodriguez, J. V., Ruohoniemi, J. M., & Van Eyken, A. P. (1999). Observations of plasma density structures in association with the passage of traveling convection vortices and the occurrence of large plasma jets. *Ann. Geophys., 17*(8), 1020-1039. doi:10.1007/s00585-999-1020-6

Wannberg, G., Wolf, I., Vanhainen, L. G., Koskenniemi, K., Rottger, J., Postila, M., . . . Huuskonen, A. (1997). The EISCAT Svalbard radar: A case study in modern incoherent scatter radar system design. *Radio Science, 32*(6), 2283-2307. doi:Doi 10.1029/97rs01803

Zhao, H. Y., Shen, X. C., Tang, B. B., Tian, A. M., Shi, Q. Q., Weygand, J. M., . . . Pu, Z. Y. (2016). Magnetospheric vortices and their global effect after a solar wind dynamic pressure decrease. *Journal of Geophysical Research-Space Physics, 121*(2), 1071-1077. doi:10.1002/2015ja021646

Zhao, H. Y., Zhou, X. Z., Zong, Q. G., Weygand, J. M., Shi, Q. Q., Liu, Y., . . . Tian, A. M. (2019). Small-Scale Aurora Associated With Magnetospheric Flow Vortices After a Solar Wind Dynamic Pressure Decrease. *Journal of Geophysical Research-Space Physics, 124*(5), 3303-3311. doi:10.1029/2018ja026234

Zhou, X. Y., Strangeway, R. J., Anderson, P. C., Sibeck, D. G., Tsurutani, B. T., Haerendel, G., . . . Arballo, J. K. (2003). Shock aurora: FAST and DMSP observations. *Journal of Geophysical Research-Space Physics, 108*(A4). doi:10.1029/2002ja009701

Zhou, X. Y., & Tsurutani, B. T. (1999). Rapid intensification and propagation of the dayside aurora: Large scale interplanetary pressure pulses (fast shocks). *Geophysical Research Letters, 26*(8), 1097-1100. doi:Doi 10.1029/1999gl900173

Zou, S., Ozturk, D., Varney, R., & Reimer, A. (2017). Effects of sudden commencement on the ionosphere: PFISR observations and global MHD simulation. *Geophysical Research Letters, 44*(7), 3047-3058. doi:https://doi.org/10.1002/2017GL072678

JGR Space Physics

Supporting Information for

Ionospheric Flow Vortex Induced by the Sudden Decrease in the Solar Wind Dynamic Pressure

Yaqi Jin[1], Jøran Idar Moen[1,2], Andres Spicher[3], Jianjun Liu[4], Lasse B. N. Clausen[1], and Wojciech J. Miloch[1]

[1]Department of Physics, University of Oslo, Oslo, Norway

[2]Arctic Geophysics, University Centre in Svalbard, Longyearbyen, Norway

[3]Department of Physics and Technology, UIT the Arctic University of Norway, Tromsø, Norway

[4]SOA Key Laboratory for Polar Science, Polar Research Institute of China, Shanghai, China

Corresponding author: Yaqi Jin (yaqi.jin@fys.uio.no)

Contents of this file

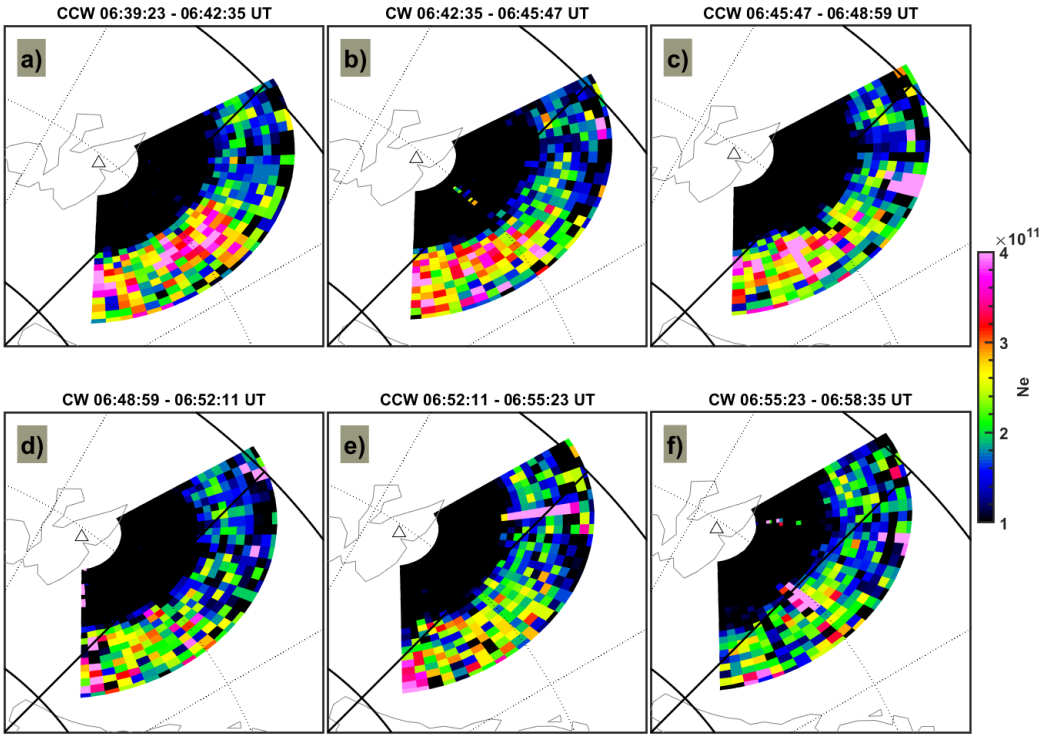

Figure S1. The electron density (Ne) profile observed by the ESR 32 m antenna. The scan time is shown on the top of each panel, where “cw” is clockwise and “ccw” is counterclockwise scan. The time period is the same as Figure 4 in the manuscript.

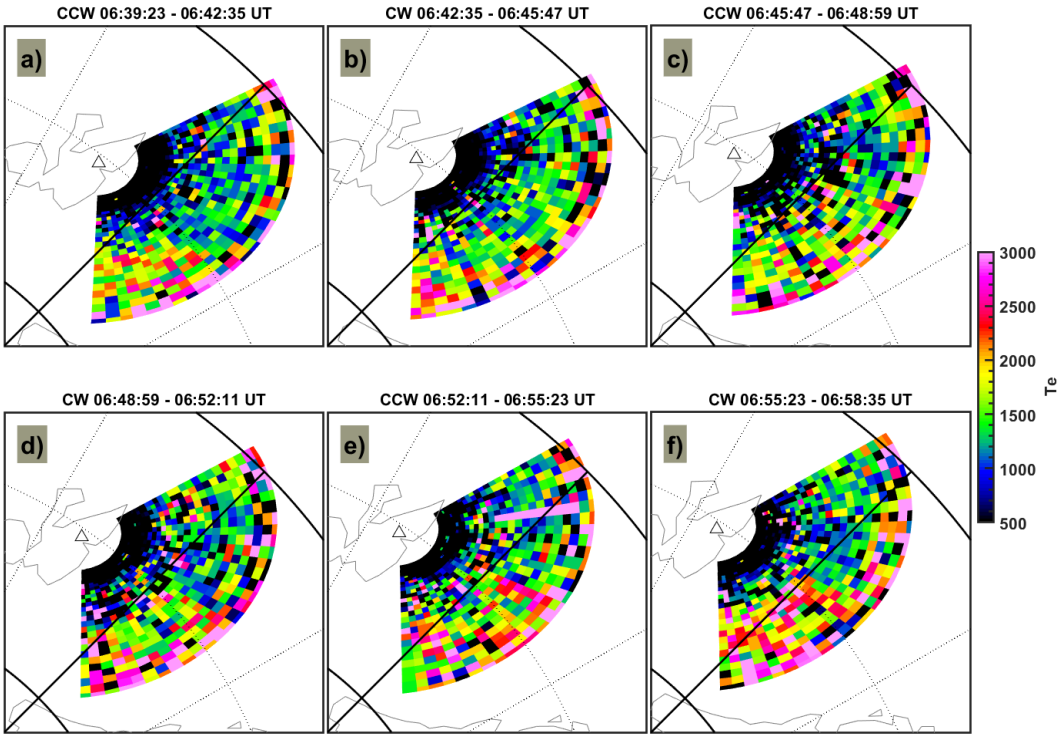

Figure S2. The electron temperature (Te) profile observed by the ESR 32 m antenna. The scan time is shown on the top of each panel, where “cw” is clockwise and “ccw” is counterclockwise scan. The time period is the same as Figure 4 in the manuscript.

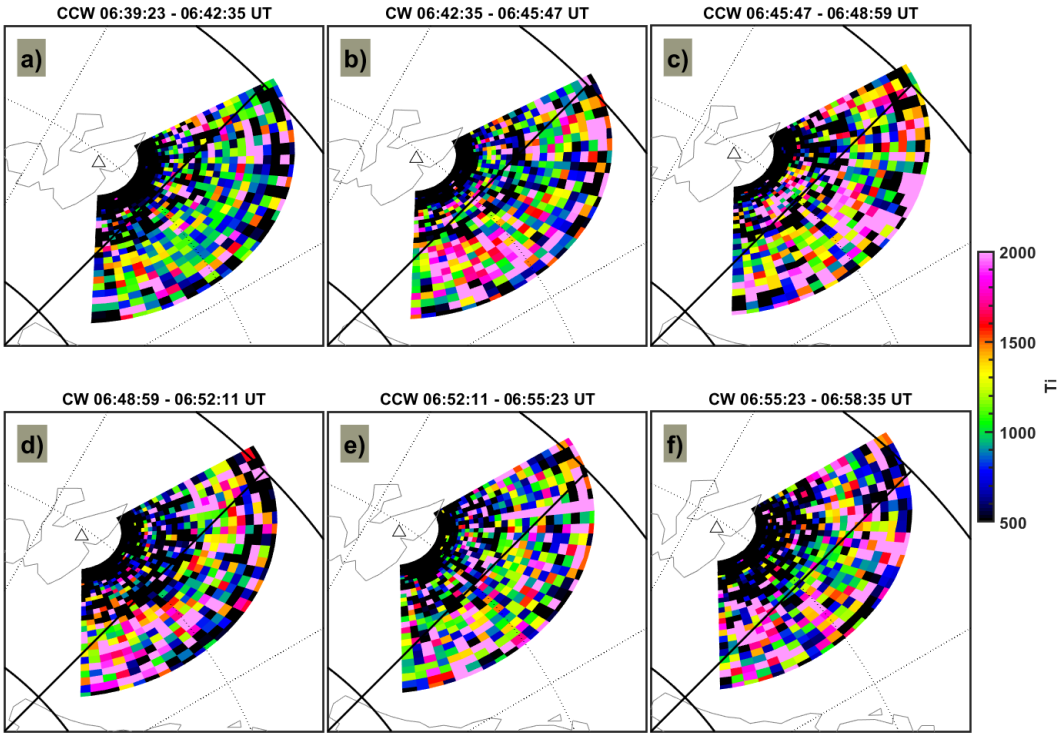

Figure S3. The ion temperature (Ti) profile observed by the ESR 32 m antenna. The scan time is shown on the top of each panel, where “cw” is clockwise and “ccw” is counterclockwise scan. The time period is the same as Figure 4 in the manuscript.